# THE IMPACT OF SATURATION ON SEISMIC DISPERSION IN SHALES - LABORATORY MEASUREMENTS.

Dawid Szewczyk[a], Rune M. Holt[a], Andreas Bauer[a,b]

**Running head**: Dispersion in shales – impact of saturation

[a] Norwegian University of Science and Technology (NTNU), Faculty of Engineering, Department of Geoscience and Petroleum, 7491, Trondheim, Norway

[b] SINTEF Petroleum Research, Formation Physics, 7465, Trondheim, Norway

Email of authors: Dawid.Szewczyk@ntnu.no

Rune.Holt@ntnu.no

AndreasKurtMarcel.Bauer@sintef.no

Corresponding author: Dawid Szewczyk

S. P. Andersens veg 15A

7031 Trondheim

Cell: +4793977810

Dawid.Szewczyk@ntnu.no

Original paper date of submission: 15 March 2017

Revised paper date of submission: 12 July 2017

ABSTRACT

Previous studies found a significant increase of acoustic velocities between seismic and ultrasonic frequencies (seismic dispersion) for shales, which would have to be taken into account when comparing seismic or sonic field data with ultrasonic measurements in the laboratory. We report on a series of experiments performed with partially saturated Mancos shale and Pierre shale I in which the influence of water saturation on acoustic velocities and seismic dispersion was investigated. The experiments were carried out in a triaxial set-up allowing for combined measurements of quasi-static rock deformation, ultrasonic velocities, and dynamic elastic stiffness at seismic frequencies under deviatoric stresses. Prior to testing, the rock samples were preconditioned in desiccators at different relative humidities. For both shale types, we present and discuss experimental results that demonstrate strong saturation and frequency dependence of dynamic Young's moduli, Poisson's ratios and Thomsen's anisotropy parameters, as well as P- and S-wave velocities at seismic and ultrasonic frequencies. The observed effects can be attributed to water adsorption and capillary pressure that are functions of several factors including water saturation. Water adsorption results in a reduction of surface energy and grain-contact stiffness. The capillary pressure affects the effective stress and possibly also the effective pore-fluid modulus, which may be approximated by Brie's empirical model. Reasonable fits to the low-frequency seismic data are obtained by accounting for these two effects and applying the anisotropic Gassmann model. The strong increase in dispersion with increasing water saturation is attributed to local flow involving adsorbed (bound) water but a quantitative description is yet to be provided.

## INTRODUCTION

A better understanding of mechanical properties of shales is of importance for various applications, including drilling (borehole stability), and production from conventional reservoirs (caprock integrity). More recently, with the production from oil and gas shales, but also with the sequestration of $CO_2$, and nuclear-waste storage in shale repositories, the interest in shales has increased strongly. Mechanical properties of shales also include acoustic velocities and their dependence on stress and fluid saturation, which is of importance in particular for seismic monitoring. Over many decades, researches have put a great effort into the investigation of the anisotropic, mechanical and acoustic properties of shales (e.g. Kaarsberg, 1959; Jones and Wang, 1981; Johnston, 1987; Vernik and Nur, 1992; Hornby, 1998; Johnston and Christensen, 1995; Wang, 2002). It is known that elastic-wave induced fluid movement in the pore space results in frequency dependant acoustic velocities in rocks, i.e. fluid saturated rocks are dispersive (e.g. Biot, 1956; White et al., 1975; Mavko and Nur, 1979; Berryman, 1988; Dvorkin and Nur, 1993; Johnson, 2001; Pride et al., 2004; Batzle et al., 2005; Duranti et. al., 2005; Batzle et al., 2006). A number of theories describing seismic dispersion and its underlying mechanisms have been proposed, however their verification remains a challenge since most experiments have been and still are performed at ultrasonic frequencies (Müller et al., 2010). Several experimental techniques for measuring acoustic velocities and attenuation in additional frequency ranges have been developed e.g. the forced deformation method for seismic frequencies (e.g. Spencer, 1981) or the resonance-bar technique for sonic frequencies (e.g. Winkler and Nur, 1979). However, the number of studies of seismic dispersion and attenuation of shales remains limited (e.g. Suarez-Rivera et al., 2001; Duranti et al., 2005; Sarker and Batzle, 2010; Delle Piane et al., 2014; Bauer et al., 2015; Mikhaltsevitch et al., 2016; Szewczyk et al., 2016). Moreover, some of the published results seem to be contradictory. Suarez-Rivera et al. (2001) measured a change in P-

wave velocity of Mancos shale in native conditions from approximately 2000 m/s at 10 Hz to above 3500 m/s in the MHz range, with a transition frequency near 10 kHz. On the other hand, Sarker and Batzle (2010) measured no significant dispersion from seismic to ultrasonic frequencies for both room dry and decane saturated Mancos samples. Therefore, to better understand dispersion in shales, systematic laboratory studies under well-defined conditions are needed.

In this work, we report on a series of experiments performed with partially saturated Mancos shale and Pierre shale I in which the influence of water saturation on seismic dispersion was investigated. The experiments were carried out in an experimental setup allowing for combined measurements of quasi-static rock deformations, ultrasonic velocities, and dynamic elastic stiffnesses at seismic frequencies under pore pressure and deviatoric stresses. Various saturations of examined samples were obtained by exposing core plugs to environments with controlled relative humidities, ranging from 12% to 100%. In addition, for Mancos shale, oven-dried samples were measured. In order to preserve the saturation states of the specimens, samples were mounted and sealed within 1 hour. After a short description of the laboratory setup, preparation technique, experimental conditions, and data processing methods, we present and discuss the experimental results including: (i) the saturation sensitivity of directional Young's moduli and Poisson's ratios as well as vertical P- and S-wave velocities for different frequency regimes, (ii) the frequency and saturation dependence of the dynamic stiffness parameters and Thomsen's parameters. We conclude our paper by discussing possible mechanisms that may explain experimental observations and comparing our measurements with the proposed poroelastic modelling.

# EXPERIMENTAL DETAILS

## Sample characterization

Mancos shale, used in this work, is an outcrop from the Western United States considered as an analogue for some shale gas reservoir rocks. XRD performed on a sample drilled from the same batch shows around 54 wt% silicate minerals (43 wt% quartz), 24 wt% clay minerals and 20 wt% carbonates (Torsaeter et al., 2012). Permeability measurements yielded a vertical gas permeability of ~6 nD – 10 nD. The porosity was not measured directly, however based on density measurements of oven-dry specimens and the mineral composition obtained from the XRD data it is estimated to be 8% ± 1%. This porosity falls within the porosity range from 1% to 11% reported for Mancos shale (Kellogg, 1977; Sarker and Batzle, 2005; Holt et al., 2012; Morsy et al., 2013). Mancos shale contains thin laminations with a fine-grained argillaceous quartz texture, and is generally assumed to exhibit transverse isotropy.

Pierre shale I, used in this work, is an outcrop shale from North Dakota considered as an analogue for some caprock formations. Pierre shale I is noticeably softer then Mancos Shale and has a higher porosity within the range ~10% - 25% (e.g. Schultz, 1964; Schultz et al., 1980; Olgaard et al., 1995; Holt et al., 2015). Core plugs were drilled from two batches of outcrop material. XRD shows that samples S15 and S19 (see Table 1) consist of about 48 wt% clay minerals, 44 wt% silicate minerals (27 wt% quartz) and around 6 wt% of carbonates. All remaining core plugs contain about 42 wt% clay minerals, 48 wt% silicate minerals (30 wt% quartz) and around 7 wt% of carbonates. Porosities of samples were not measured directly, however, based on the density measurements of as-received samples, that were nearly fully saturated (short consolidation time while exposing the core plugs to brine), and mineral density

and composition taken from XRD tests, we have estimated the porosity of 16% ± 1%. Pierre shale I is commonly assumed to be transverse isotropic (e.g. Schultz et al., 1980).

**Sample preparation and experimental conditions**

Eleven cylindrical Mancos shale core plugs with a diameter of one inch and length of two inches, and eight cylindrical Pierre shale I core plugs of the same size were cut from outcrop material preserved in oil. To assess the anisotropic properties of the shales, experiments were performed with differently oriented samples: The angle between the sample axis and the symmetry axis of the shale (normal to bedding) was $0^o$, ~$45^o$ and $90^o$ (see Table 1). As-received samples (corresponding to around 76% saturation in case of Mancos shale and close to full saturation in case of Pierre shale I) were placed inside desiccators in which the relative humidity (RH) was controlled by saturated solutions of different types of salts (Greenspan, 1977) given in Table 1. Actual RH was measured by hygrometers placed inside the desiccators. The samples were put into the desiccators after the RH had stabilized. The specimens were stabilizing under room temperature, and their weight was controlled once per day. Samples exposed to different RH were either gaining or losing weight and expanding or shrinking slightly (see Figure 1 and Table 1) depending on the initial state of the core plugs and RH that they have been exposed to. Experiments were performed after the weight of samples did not change by more than 0.01 g over the course of 1 week.

[Figure 1 about here]

All tests performed with both Pierre shale and Mancos shale were conducted under deviatoric stress, under drained conditions, and at room temperature. For Mancos shale, the confining stress was $P_{conf} = 17\ MPa$, the axial stress was $\sigma_{ax} = 26\ MPa$. For Pierre shale I, the

confining stress was $P_{conf} = 18.5\ MPa$, the axial stress was $\sigma_{ax} = 20\ MPa$. Neither for Mancos shale nor Pierre shale was any pore pressure applied (pore-fluid lines were open during loading and subsequently sealed to prevent exposure to a different RH). Loading rates were 10 $MPa/h$ and 5 $MPa/h$ for Mancos shale and Pierre shale, respectively.

[Table 1 about here]

**Experimental set-up and sample handling**

The experiments were performed in the Formation Physics laboratory at SINTEF Petroleum Research, within a triaxial compaction cell allowing for simultaneous measurements of quasi-static deformations of core plugs, ultrasonic velocities (P- and S-wave velocities in axial direction), and dynamic elastic properties (Young's modulus and Poisson's ratio) at seismic frequencies (0.1 Hz – 150 Hz) under deviatoric stresses. Conceptually, the apparatus is comparable to the setup at Colorado School of Mines (Batzle et al., 2006) with few modifications, including: (i) fast sample mounting (~ 1 hour); (ii) independent control of axial stress, radial stress and pore pressure; and (iii) static-deformation measurements. A schematic drawing of the cell together with sample stack is shown in Figure 2.

[Figure 2 about here]

The sample stack consists of a rigid piston, two endcaps with the sample placed between them, an aluminium piece with semiconductor strain gages (used for phase shift measurements at seismic frequencies), a piezoelectric force sensor (Kistler), a piezoelectric actuator (PI), and an internal load cell (MetaRock). The entire column is mounted on the base flange of the compaction cell equipped with fluid lines for confining and pore pressure control as well as necessary electric feedthroughs. The compaction cell is placed inside a mechanical loading frame

(MTS) that exerts axial force on the sample stack. Both top and bottom endcaps are equipped with a pair of in-house built compressional (P) and shear (S) wave transducers (500 kHz centre frequency) which allows for determination of velocities by the use of pulse-transmission technique. Endcaps are also equipped with pore-fluid lines that allow for pore fluid substitution/pore pressure control. The static axial deformation of the entire sample is measured by three linear variable displacement transducers (LVDT) mounted in between the endcaps (equally distributed around the circumference of the core plug). To verify the deformation measurements and to exclude possible large heterogeneities of the sample (that would create local strain variations), the LVDT readouts are compared with the signals obtained from the strain gages attached to the sample. Afterwards static deformation data together with force measurements provided by the internal load cell are used to determine quasi-static properties of the tested core plugs. Finally, the determination of elastic parameters at seismic frequencies is achieved by utilizing the forced deformation method (Spencer, 1981), with small-amplitude axial strain oscillations ($< 10^{-6}$) measured locally on the samples by strain gages, and force oscillations measured by a force sensor integrated in the sample stack. In order to decrease the time the samples were exposed to ambient conditions during mounting (which could lead to the change of saturation) instead of gluing the strain gages to the sample's surface, the gages were taped onto the surface and the mechanical coupling between gage and sample was provided by the applied confining pressure. This approach allowed for strain gage mounting and subsequent sample sealing within 1 hour after removing the core plugs from the desiccators. Details and validation of this procedure together with a detailed description of the setup is given in Szewczyk et al. 2016.

**Sources and magnitudes of experimental errors**

The errors in the ultrasonic velocity measurements associated with: (i) picking of the arrivals, (ii) possible misalignment of the ultrasonic transducers with respect to the bedding, (iii) interface are estimated to be between 2 – 5 %. The errors in the seismic frequency measurements are associated with the following possible sources: (i) non-parallel alignment of the strain gages with respect to the sample axis, (ii) small misalignment of the stack (decreasing with increasing confining pressure), (iii) energy dissipation due to friction between the rubber jacket and the confining pressure oil, (iv) electronic noise, and (v) sample bulging. Resulting errors were estimated based on the seismic-frequency measurements of the Young's modulus and the Poisson's ratio performed with non-dispersive standard materials (aluminium and PEEK). For both standard materials, the experimental errors did not exceed 5%. In addition, since the core plugs were not tested under hydrostatic pressure (additional axial stress applied), based on the stress sensitivity studies reported in Szewczyk et al. (2017), a small 1 – 2 % error associated with different stress states of $0^o$, $45^o$ and $90^o$ oriented samples is expected in measured seismic and ultrasonic moduli. The errors associated with heterogeneities of the samples leading to local strain variations on a scale larger than the size of the strain gages (e.g. inaccuracy during drilling or internal variations of lamination - see Fig 7d) may introduce additional errors (see "Role of a bedding angle" section). Our sensitivity studies of the TI material has shown that while converting from ultrasonically measured velocities to engineering parameters (see "data analysis procedure" section), a $10^o$ orientation error for a nominally $45^o$-oriented sample, may lead to an 11% error in determination of vertical Young's modulus and around ±0.07 error in determination of Poisson's ratio. While converting from moduli measured at seismic frequencies to velocities similar sensitivity studies shows 8% error in determination of vertical S-wave velocity, whereas P-wave velocity is not affected by orientation errors of nominally $45^o$-oriented sample.

# D ATA ANALYSIS PROCEDURE

## Conversion between engineering parameters and elastic velocities in TI media

Measurements performed at seismic and ultrasonic frequencies produce two different sets of dynamic properties. While the forced deformation method determines directional Young's modulus, E, and Poisson's ratio, $\nu$, the pulse-transmission technique provides the P- and S-wave velocities. Therefore, comparison of obtained results requires conversion between those types of parameters. In elastic materials, stress, $\sigma_{ij}$, and strain, $\varepsilon_{kl}$ , tensors are related by Hooke's law:

$$\sigma_{ij} = C_{ijkl}\varepsilon_{kl} \tag{1}$$

where $C_{ijkl}$ denotes the elastic stiffness matrix and Einstein's summation convention applies. In a transverse isotropic material, the stiffness matrix is composed by five independent parameters (e.g. Nye, 1985):

$$C_{ij} = \begin{bmatrix} C_{11} & C_{11}-2C_{66} & C_{13} & 0 & 0 & 0 \\ C_{11}-2C_{66} & C_{11} & C_{13} & 0 & 0 & 0 \\ C_{13} & C_{13} & C_{33} & 0 & 0 & 0 \\ 0 & 0 & 0 & C_{44} & 0 & 0 \\ 0 & 0 & 0 & 0 & C_{44} & 0 \\ 0 & 0 & 0 & 0 & 0 & C_{66} \end{bmatrix} \tag{2}$$

here the z-axis is the unique symmetry axis and Voigt notation (Voigt, 1928) applies.

The anisotropy of the material can be quantified by three parameters introduced by Thomsen (1986):

$$\varepsilon = \frac{C_{11}-C_{33}}{2C_{33}} \tag{3}$$

$$\gamma = \frac{C_{66}-C_{44}}{2C_{44}} \tag{4}$$

$$\delta = \frac{(C_{13}+C_{44})^2-(C_{33}-C_{44})^2}{2C_{33}(C_{33}-C_{44})} \tag{5}$$

The independent stiffnesses ($C_{11}$, $C_{33}$, $C_{44}$, $C_{66}$, $C_{13}$) fully characterize the TI material, and any of its properties may be calculated with the proper combination of those parameters (e.g. Helbig, 1994; Mavko et al., 2009) i.e.

a) Elastic velocities:

$$V_{PV} = \sqrt{\frac{C_{33}}{\rho}} \tag{6}$$

$$V_{SV} = \sqrt{\frac{C_{44}}{\rho}} \tag{7}$$

$$V_{PH} = \sqrt{\frac{C_{11}}{\rho}} \tag{8}$$

$$V_{SH} = \sqrt{\frac{C_{66}}{\rho}} \tag{9}$$

$$V_{qP}(\theta) = \sqrt{\frac{C_{11}sin^2\theta + C_{33}cos^2\theta + C_{44} + \sqrt{[(C_{11}-C_{44})sin^2\theta - (C_{33}-C_{44})cos^2\theta]^2 + 4[C_{13}+C_{44}]^2 sin^2\theta cos^2\theta}}{2\rho}} \tag{10}$$

$$V_{qS}(\theta) = \sqrt{\frac{C_{11}sin^2\theta + C_{33}cos^2\theta + C_{44} - \sqrt{[(C_{11}-C_{44})sin^2\theta - (C_{33}-C_{44})cos^2\theta]^2 + 4[C_{13}+C_{44}]^2 sin^2\theta cos^2\theta}}{2\rho}} \tag{11}$$

where ρ denotes bulk density, P and S stands for compressional and shear waves respectively, while $V_{qP}(\theta)$ and $V_{qS}(\theta)$ represents phase velocity of "quasi P-waves" and "quasi S-waves" i.e. waves with the wave-vector normal oriented at an angle θ with respect to material symmetry axis. The direction of the symmetry axis is denoted by subscript V, while subscript H denotes directions within the symmetry plane.

b) Engineering parameters:

$$E_V = C_{33} - \frac{C_{13}^2}{C_{11}-C_{66}} \tag{12}$$

$$\nu_{VH} = \frac{C_{13}}{2(C_{11}-C_{66})} \tag{13}$$

$$E_H = \frac{4C_{66}[(C_{11}-C_{66})C_{33}-C_{13}^2]}{C_{11}C_{33}-C_{13}^2} \quad (14)$$

$$\nu_{HV} = \frac{2C_{66}C_{13}}{C_{11}C_{33}-C_{13}^2} \quad (15)$$

$$\nu_{HH} = \frac{(C_{11}-2C_{66})C_{33}-C_{13}^2}{C_{11}C_{33}-C_{13}^2} \quad (16)$$

$$\frac{1}{E(\theta)} = \frac{cos^4\theta}{E_V} + \frac{sin^4\theta}{E_H} + \frac{sin^2\theta cos^2\theta[(C_{11}-C_{66})C_{33}-(C_{13}+C_{44})C_{13}]}{C_{44}[(C_{11}-C_{66})C_{33}-{C_{13}}^2]} \quad (17)$$

Therefore, the conversion between data obtained at seismic and ultrasonic frequencies can be performed when experiments provide enough information to determine all independent stiffnesses. In conventional compaction cells, where only biaxial stresses can be applied (axial stress and confining pressure) and only axial properties measured, determination of independent $C_{ij}$'s requires repetitions of the experiment on samples drilled at three different angles of inclination with respect to the bedding ($0^o$, $90^o$, and at least one additional oblique angle). Afterwards, equations 6-17 may be inverted for the independent stiffness parameters characteristic for a given frequency and then re-used to determine property of interest.

In the present work, due to the limited number of available core plugs, the procedure described above was applied in the following cases: (i) Mancos shale – RH = 12% and RH = 86%; (ii) Pierre shale I – RH = 19% and RH = 55%. The independent stiffnesses of the remaining core plugs were determined from the measured vertical properties and the Thomsen's parameters obtained by linear extrapolation of ε, γ and δ vs RH curves, determined for saturations for which three differently oriented core plugs were tested. The equations allowing to determine independent stiffnesses from this set of data, were obtained by inverting equations 3-5 and equations 6-7 (for ultrasonic frequencies) or equations 3-5 and equations 12-13 (for seismic frequencies). This procedure leads to two independent solutions. The choice of the physically

valid solution was dictated by the following inequalities that are a consequence of the requirement of positive elastic energy (e.g. Nye, 1985):

$$C_{44} > 0;\ C_{66} > 0;\ C_{33} > 0;\ C_{11} > C_{66} > 0;\ (C_{11} - C_{66})C_{33} - C_{13}^2 > 0 \quad (18)$$

**Determination of saturation level**

In order to convert the relative humidities into saturations we have used the mineral density and the XRD composition of both Mancos shale and Pierre shale. For both shale types, we have calculated expected density in the fictitious case of zero porosity. For Mancos shale, this density was compared with the measured bulk density of the oven-dried sample, and porosity was calculated under the assumption that the oven-dry specimen represents saturation equal to 0.02 (drying of the shales under 105$^{o}$C does not allow for the evaporation of fluid absorbed in the thin clay layer or in small non-connected pores - Chenevert and Amanullah (1997)). In the case of the Pierre shale, calculated density was compared with the measured bulk density of as-received samples (which were close to full saturation) and the porosity was calculated under the assumption that as-received samples represents saturation of 98%. Finally, the saturation level was calculated by comparing the total available pore volume (obtained from determined porosities) with the volume of water corresponding to the mass change measured during drying of samples (see Figure 1). During saturation calculations, the change of volume of samples during stabilization in desiccators leading to the change of the pore volume was taken into account. Described procedure resulted in the RH to saturation conversion shown in Table 1.

## E XPERIMENTAL RESULTS

Experimental data are shown in Figures 3-17 and the numerical values of seismic frequency measurements (for frequencies of 1 Hz, 21 Hz and 105 Hz) and ultrasonic measurements are tabulated in Appendix D.

**Seismic Young's moduli and Poisson's ratios, and ultrasonic velocities**

Figure 3 and 4 show the directly measured directional seismic Young's moduli and Poisson's ratios, as well as ultrasonic velocities of partially saturated Mancos shale and Pierre shale for which three different orientations of the core plugs were available.

[Figure 3 about here]

[Figure 4 about here]

Figure 3 (a-e) and Figure 4 (a-e) show that both Mancos shale and Pierre shale exhibit considerable dispersion in all directional Young's moduli and nearly no dispersion in the directional Poisson's ratios at seismic frequencies (1 – 155 Hz). The figures also reveal features that are characteristic for TI media: (i) seismic Young's moduli and ultrasonic P- and S-wave velocities for loading parallel to bedding ($E_H$, $V_{PH}$, $V_{SH}$) are significantly higher than those obtained for loading perpendicular to bedding ($E_V$, $V_{PV}$, $V_{SV}$); (ii) seismic Young's moduli and ultrasonic P- and S-wave velocities for loading under an oblique angle to bedding ($E_{45^o}$, $V_{qP}$, $V_{qS}$) are in between data obtained for loading parallel and perpendicular to bedding; (iii) seismic Poisson's ratios obtained with the 0° sample, $\nu_{VH}$, lies in between the two Poisson's ratios obtained with the 90° sample, $\nu_{HH}$ and $\nu_{HV}$. Furthermore, for TI media, symmetry of the compliance matrix requires:

$$\frac{\nu_{VH}}{E_V} = \frac{\nu_{HV}}{E_H} \tag{19}$$

As indicated in Figures 3 (e) and 4 (e), within the error of the measurements, Eq. 19 is confirmed by our measurements. This shows that both Mancos shale and Pierre shale can be described as transversely isotropic materials. In addition, the fact that Eq. 19 is fulfilled for all frequencies (despite observed dispersion) gives confidence in the applied experimental techniques.

Figure 5 and 6 show the saturation dependency of some of the directly measured seismic vertical Young's moduli and Poisson's ratios, as well as ultrasonic vertical P- and S-wave velocities of Mancos shale and Pierre shale core plugs.

[Figure 5 about here]

[Figure 6 about here]

For both shale types, a strong and qualitatively similar saturation dependence of the seismic Young's moduli and Poisson's ratios as well as ultrasonic P- and S-wave velocities can be observed. At seismic frequencies, an increase in water content results in a strong softening of the shale and increases Young's modulus dispersion. Mancos shale become around 27% softer when going from oven-dried samples to 100% RH, while for Pierre shale, $E_V$ is reduced by about 17% when going from RH = 19% to RH = 76%. Dispersion at seismic frequencies is represented by the separation between different presented frequencies. Poisson's ratio increases by about a factor of four between dry and moist samples. In case of Mancos shale, the vertical Poisson's ratio gradually increases from about 0.08 at 12% RH to about 0.3 for 100% RH. In case of Pierre shale, Poisson's ratio changes from around 0.1 at 19% RH up to about 0.25 for RH = 76%. Overlapping of the curves representing different frequencies, indicate nearly no dispersion in vertical Poisson's ratios at seismic frequencies. Note however, that for Pierre shale an increase in water content beyond about 50% saturation causes a slight increase of the dispersion.

Qualitatively similar effects of an increased water saturation on seismic Young's moduli and Poisson's ratios were observed before for Mancos shale by Bauer et al., (2015) (1Hz – 155 Hz) and Mikhaltsevitch et al., (2016) (0.1 Hz – 100 Hz). Both of them reported on rather strong softening of the studied core plugs followed by an increased dispersion of Young's modulus with additional water content. They have also observed high increase of Poisson's ratios with increased saturation. Note however, that the core plugs tested by Mikhaltsevitch et al., (2016) seem to be softer than presented here, they also exhibits smaller $E_V$ dispersion for core plugs exposed to RH < 60%. In addition, Mikhaltsevitch et al., (2016) reported on increasing dispersion of Poisson's ratios of Mancos shale with increased water content, whereas we observe similar effect for Pierre shale only.

Ultrasonic vertical P- and S-wave velocities of both shale types exhibit large non-monotonous saturation dependence. Elastic velocities are lower in Pierre shale than in Mancos shale, but saturation dependencies are qualitatively similar. Vertical P-wave velocities of relatively dry samples (up to ~ 30% saturation) drop slightly with increasing saturation. For higher water saturations, ultrasonic $V_{PV}$ exhibits a strong increase up to ~ 70% saturation. Beyond this saturation $V_{PV}$ in Mancos shale drops slightly (similar phenomenon was also observed in Tournemire shale by Vales et al. (2004)). For S-wave velocities, again a slight decrease of $V_{SV}$ with saturation can be observed for relatively dry samples (up to ~ 30% saturation). As the saturation further increases the ultrasonic S-wave velocities slightly increase up to ~ 70% saturation before they slightly drop again in Mancos shale, which is qualitatively similar to the saturation dependence of the ultrasonic P-wave velocities (for Pierre shale, there is no data available for water saturation > 70%).

## LINKING SEISMIC AND ULTRASONIC DATA

**Role of a bedding angle**

In order to compare the shale properties acquired at seismic and ultrasonic frequencies, the conversion between engineering parameters and elastic velocities in TI media described in "Data analysis procedure" section is needed. For ultrasonic frequencies, while converting directly measured velocities to engineering parameters, $C_{13}$ affects all directional Young's moduli and Poisson's ratios (accordingly to equations 12-17). For seismic frequencies, while converting directly measured engineering parameters to elastic velocities, $C_{44}$ affects vertical S-wave velocity as well as both "quasi-P-" or "quasi-S-" wave velocities (accordingly to equations 7 and 10-11). In our experiments, the value of $C_{13}$ at ultrasonic frequencies, and the value of $C_{44}$ at seismic frequencies is determined based on direct measurements of $V_{qP}$, $V_{qS}$ and $E(\theta)$, respectively. These measurements are performed with samples drilled at 45° angle with respect to the bedding plane and independent stiffnesses are calculated from equations 10-11 and 17. Due to the steep slopes of trigonometric functions around 45°, unavoidable internal variation of lamination orientation and/or inaccurate cutting of the core plugs can result in relatively large errors. Similarly, heterogeneities between differently oriented samples also affect the conversion between different rock properties. Figures 7 and 8 shows the sensitivity of engineering parameters ($E_V$, $\nu_{VH}$) and S-wave velocity ($V_{SV}$) calculated from ultrasonic and seismic measurements respectively, to a deviation from the nominal angle of 45°. In Figures 7 (a,b) and 8 (a,b) ultrasonic velocities measured with samples drilled at 0°, 45° and 90° angle with respect to bedding were used to determine the TI stiffness matrix and then converted to vertical Young's modulus and Poisson's ratio. In Figures 7 (c) and 8 (c) seismic Young's moduli and Poisson's ratios measured with three differently oriented samples were used to determine the TI stiffness matrix and then converted to vertical S-wave velocity.

[Figure 7 about here]

[Figure 8 about here]

Figures 7 and 8 reveals that a relatively small sample orientation error ($\pm 10^{O}$) results in large variations of the calculated Young's moduli, Poisson's ratios and S-wave velocities. Since it is difficult to determine the actual (average) sample orientation or to quantify the possible effects of the heterogeneities, and since we obtained in some cases non-physical results when assuming the nominal angle of 45°, we slightly adopted this angle within the error margins in order to fulfil the following requirement: (i) the dispersion of the vertical Young's modulus, $E_V$, should not be negative ($E_V$ increase with frequency), and (ii) the vertical Poisson's ratio, $\nu_{VH}$, should exhibit only small (or none) dispersion from seismic to ultrasonic frequencies (the critical frequency is independent of the measured property and Poisson's ratio exhibits hardly any dispersion at seismic frequencies, simultaneously Young's modulus shows significant dispersion between 1 Hz – 155 Hz, thus Poisson's ratio should exhibit small (or none) dispersion from seismic to ultrasonic frequencies). In this way, the sample orientation of the samples with a nominal angle of 45° were set to: 55° for RH = 12% Mancos shale, 45° for RH = 86% Mancos shale, 39° for RH = 19% Pierre shale, and 33° for RH = 55% Pierre shale.

Note that the determination of the seismic vertical P-wave velocity from the directly measured directional Young's moduli and Poisson's ratios is not affected by this procedure, since $C_{33}$ can be calculated with the use of the properties of 0° and 90° oriented samples, only. In the following, we will directly indicate which of the presented data were affected by assuming a change of the nominal oblique angle, and which were not.

**Frequency dependence of stiffness and velocity anisotropy**

The measurement of Young's modulus and Poisson's ratio as well as axial P- and S-wave velocities for three different sample orientations allows for a full characterization of stiffness and velocity anisotropy. Figure 9 shows frequency dependence of velocity anisotropy (Thomsen's anisotropy parameters) in Mancos shale and Pierre shale, obtained for the saturations for which three differently orientated samples were available. Values of ε at seismic and ultrasonic frequencies and values of γ at ultrasonic frequencies are not affected by the procedure described in "Role of a bedding angle" section.

[Figure 9 about here]

For Mancos shale, at seismic frequencies, both ε and γ decrease while δ increases with increasing frequency. Increased saturation causes large increase of δ but only a slight increase of ε and γ. Thomsen's parameters determined for Pierre shale show a different behaviour. Within the seismic range, for Pierre shale exposed to RH = 19%, the values of ε and γ remain nearly constant while δ decreases. Differently from Mancos shale, increased saturation has a small impact on the values of all Thomsen's parameters. Note however, that additional water content seem to change the trend of δ at seismic frequencies.

Figure 10 shows the frequency dependence of five independent stiffness parameters $C_{11}$, $C_{33}$, $C_{44}$, $C_{66}$ and $C_{13}$ of the Mancos shale and Pierre shale measured for the saturations for which three differently orientated samples were available. Values of $C_{11}, C_{33}$ and $C_{66}$ at both seismic and ultrasonic frequencies, values of $C_{13}$ at seismic frequencies, and values of $C_{44}$ at ultrasonic frequencies are not affected by the procedure described in "Role of a bedding angle" section.

[Figure 10 about here]

For both shale types, highest dispersion is observed for $C_{11}$ and $C_{33}$. As the saturation increases, the $C_{11}$ and $C_{33}$ slightly decrease at seismic frequencies for both shales. In contrast, at ultrasonic frequencies, additional water content causes an increase of $C_{11}$ and $C_{33}$ as a result of enhanced dispersion. Both $C_{44}$ and $C_{66}$ decrease with increasing saturation in both frequency regimes, but the dispersion of $C_{44}$ and $C_{66}$ is hardly affected by saturation changes.

Frequency dependence of the stiffness parameters, $C_{ij}$'s, obtained from measurements with $0^O$-oriented samples (by using extrapolated Thomsen's parameters) are shown in Figure 11 and Figure 12 for Mancos shale and Pierre shale I, respectively.

[Figure 11 about here]

[Figure 12 about here]

For both shale types, some common features are found: (i) the highest dispersion is observed for $C_{11}$ and $C_{33}$; (ii) as saturation increases (up to RH = 76%) $C_{11}$ and $C_{33}$ decrease at seismic frequencies and increase at ultrasonic frequencies; (iii) $C_{44}$ and $C_{66}$ exhibit relatively small dispersion; (iv) dispersion of $C_{44}$ and $C_{66}$ slightly increases with increasing saturation; (v) both $C_{44}$ and $C_{66}$ decrease with increasing saturation (effect much higher for Pierre shale). For relatively dry samples of both shale types, $C_{13}$ has the lowest value compared to the other stiffness parameters. As the saturation increases, $C_{13}$ increases and become comparable to or even higher than $C_{44}$ and $C_{66}$.

**Dispersion and saturation dependence of vertical Young's modulus and Poisson's ratio**

Figures 13 and 14 show the saturation dependence of vertical Young's modulus, $E_V$, and Poisson's ratio, $\nu_{VH}$, of Mancos shale and Pierre shale for different frequency regimes. Data points at seismic frequencies were measured directly, ultrasonic data were determined from

velocity measurements and were affected by procedure described in "Role of a bedding angle" section.

[Figure 13 about here]

[Figure 14 about here]

Both shale types exhibit strong saturation sensitivity of the vertical Young's modulus and Poisson's ratio. Figures 13 and 14 show that all previously showed saturation dependencies of the low frequency $E_V$ and $\mathcal{V}_{VH}$ can be extrapolated to all measured seismic frequencies. At the same time, additional water content results in large increase of dispersion between seismic and ultrasonic regimes. For Mancos shale, $E_V$ increases by more than 50% between 1 Hz and ultrasonic frequencies for the 100% RH sample, while the 12% RH or oven-dried samples exhibit only minor dispersion. For Pierre shale, an increase in $E_V$ of more than 50% between seismic and ultrasonic frequencies is already observed at RH 76%, while smaller saturations exhibit again small dispersion. At ultrasonic frequencies, the rock softening effect visible at seismic frequencies is still present. However, it is superposed by the dispersion effects, which results in a rather complex water-saturation dependence. Up to ~RH = 34%, an increase in water saturation causes $E_V$ to decrease for both shale types. This decrease is followed by a stiffening of the samples up to ~ RH = 76% (mainly due to increased dispersion in this saturation range). Beyond RH = 76%, the dispersion is not increasing much, and the softening effect again dominates. The large, gradual increase of the vertical Poisson's ratio with saturation, observed at low frequencies, is also visible at ultrasonic frequencies. The ultrasonic and seismic values of the Poisson's ratios are roughly comparable indicating rather small, saturation independent dispersion (beside relatively moist samples). Solid lines in Figures 13 and 14 (a) correspond to the manual Cole-Cole fits (Appendix B) of the measured vertical Young's moduli, and dashed

lines represent the corresponding attenuation (best fits were obtained for $\alpha = 0.65$). The inverse of the quality factor was not measured directly during our experiments, note however, that under the assumption that the Cole-Cole model provides the physically meaningful predictions for anisotropic rocks, the Cole-Cole fits indicate that the seismic dispersion at low water saturation ($RH \leq 34\%$) exhibits peak of attenuation in the seismic band, while samples with more pronounced dispersion ($RH \geq 76\%$) seem to have a characteristic frequency in the sonic band.

**Dispersion and saturation dependence of the elastic velocities**

Figures 15 and 16 show the effect of water saturation on the seismic and ultrasonic vertical P- and S-wave velocities. Ultrasonic points were measured directly while velocities at seismic frequencies were calculated from measured Young's moduli and Poisson's ratios. Note however, that only seismic S-wave velocities were affected by procedure described in"Role of a bedding angle" section.

[Figure 15 about here]

[Figure 16 about here]

Figures 15 and 16 expand previously observed large, qualitatively similar in both shales, non-monotonous saturation dependence of velocities to seismic frequencies. Figures 15 and 16 show however that the saturation dependency of the P- and S-wave velocities is different at seismic and ultrasonic frequencies. Vertical P-wave velocities of relatively dry samples (up to ~ 30% saturation) drop slightly with increasing saturation at both ultrasonic and seismic regimes. For higher water saturations, the difference between seismic and ultrasonic velocities increases, thus indicating the increase of the dispersion with increased saturation. At seismic frequencies, the vertical P-wave velocity changes only slightly up to~50% saturation, and increases at higher

saturations. At ultrasonic frequencies, $V_{PV}$ exhibits a strong increase up to ~ 70% saturation and drops slightly afterwards. This results in a complex dispersion behaviour, with the highest dispersion around 70% water saturation and smallest for relatively dry samples. For S-wave velocities, dispersion is also evident for higher saturations. Again, for relatively dry samples (up to ~ 30% saturation) of both shales, $V_{SV}$ slightly decreases with saturation at both seismic and ultrasonic frequencies, and only small dispersion can be observed. As the saturation increases the seismic S-wave velocities continues to decrease, while the ultrasonic S-wave velocities slightly increase up to ~ 70% saturation and drop afterwards, thus indicating that (as for P-wave velocities) the dispersion is smallest for relatively dry samples and larger for the moist ones.

## INTERPRETATION OF EXPERIMENTAL RESULTS

### Water adsorption and capillary-pressure effects

There are good reasons to believe that the observed saturation dependence of the stiffness and the stiffness/velocity dispersion of Mancos and Pierre shale can to a large extent be attributed to both water adsorption effects and capillary-pressure effects. In sedimentary rocks, the pore fluid and physicochemical interactions have a strong impact on the petrophysical rock properties. In the present experiments, the relative humidity (RH) is a control parameter that is directly related to the total suction (or chemical potential of water), $s_t$ (Tarantino, 2010):

$$s_t = \frac{RT}{V_m}\ln(RH) \tag{20}$$

where R is the gas constant, T is the temperature, and $V_m$ is the molar volume of water. The total suction is a sum of matric suction, including capillary and adsorption (electrostatic) effects, and solute suction given by the solute (salt) concentration in the pore fluid. Both capillary pressure

and water adsorption affect the rock stiffness, which means that a change in relative humidity will result in a stiffness change.

Since a change in relative humidity results in a change of water content, stiffness changes may also be induced by salt precipitation (during dry-out). Moreover, a change in pore-water salinity with changing water content (the salt content in the sample is fixed) will result in a change in solute suction and hence a change in matric suction (since the total suction is fixed at a given RH), which would have to be accounted for in a quantitative description. Changes in the stiffness can also be caused by desiccation or swelling-induced rock damage (e.g. desiccation cracks).

Both salt-precipitation effects and rock-damage effects could be the subject of further, more systematic studies. For the study of the latter, it is recommended to expose a given sample to several cycles of decreasing and increasing RH in order to find out if the observed stiffness variations are reversible or caused by irreversible rock damage. Ideally, such cycles should be performed under confining stress since damage effects might be stronger at low confining stress. It should be noted however, that for both Pierre shale and Mancos shale, the rock stiffness measured in this work shows a clear and repeatable correlation with RH irrespective of whether the sample loses or gains water. Mancos shale, e.g., gains water when exposed to 100% RH and loses water when exposed to RH $\leq$ 75%. While the low frequency Young's modulus decreases when exposed to 100% RH, it increases during dry-out. If the stiffness changes would be due to rock damage one might have expected a rock softening in both cases.

In the following, we will discuss the capillary-pressure effects and adsorption effects and whether they can explain (at least qualitatively) the observed changes in stiffness and dispersion.

Capillary pressures are known to influence the rock stiffness. The capillary pressure, $p_c$, is given by

$$p_c = \frac{2\,\gamma cos\theta}{r}\ , \qquad (21)$$

with γ being the surface tension, θ the contact angle, and r the radius of curvature of the meniscus. In the present case, water is the wetting phase and air the non-wetting phase, and the pressure in the water phase, $p_w$, is smaller than the pressure in the air, $p_a$: $p_a - p_w = p_c$. The capillary-pressure contribution to the total suction, $s_t$, in Eq. 20, is given by $-p_c$. With decreasing RH, the water content decreases, and the radius of the water menisci is reduced. For estimating the effect of the capillary pressures on the rock stiffness, an effective pore pressure, $p_{eff}$, that acts against the total stress is often applied (Bishop's law):

$$p_{\text{eff}} = p_a - \chi(p_a - p_w) \qquad (22)$$

where χ is a constant that depends on the degree of saturation. The effective stress, σ', i.e. the stress acting on the rock matrix and causing stiffness changes, is given by $\sigma' = \sigma - p_{eff}$. In the simplest case, χ is equal to the wetting-phase saturation (here the water saturation), which means that the effective pore pressure is the average of the wetting and non-wetting phase pressures weighted by the respective saturations. By reducing the relative humidity, the pressure in the water phase (strongly) decreases, resulting in enhanced effective stresses and rock stiffening. However, by approaching zero water saturation, the effective pore pressure would again converge to the gas pressure despite very large capillary pressures. The experimental results obtained with Mancos shale suggest that the rock samples gradually stiffen (at seismic frequencies) with decreasing RH, with the oven-dried sample exhibiting the highest Young modulus. This may still be consistent with Bishop's law since the water saturation of the oven-dried sample is not zero, and there might be a more complex dependence of χ on water

saturation. However, if rock stiffening would be due to an increase in effective stress alone (assuming that the effective-stress concept applies) one would expect that Young's modulus and Poisson's ratio should behave in a similar way by increasing the total confining stress at constant RH. We have performed such experiments with Mancos shale and observed that Poisson's ratio increases when increasing the confining stress, while in the present experiments, Poisson's ratio decreased with decreasing RH, i.e. increasing effective stress. Therefore, we conclude that rock stiffening during a reduction of RH cannot be explained by capillary pressures alone, or that Bishop's law does not apply. Capillarity might however play a role in controlling the effective bulk modulus of the pore fluid (Santos et al., 1990), which could explain the observed saturation dependence of Poisson's ratio as discussed in the next paragraph.

We think that adsorption effects explain (or partly explain) the observed effects of softening with increasing RH, in accordance with previous findings (Spencer, 1981; Moerig et al., 1996; Murphy et al., 1984). Adsorption of water on the grain surfaces results in a gradual reduction of grain-surface energy and increase in water-layer thickness if the relative humidity is increased from zero to 100% (Murphy et al., 1984). For the contact of spherical particles (Hertz-Mindlin model), Johnson et al. (1971) showed that the contact area between grains depends on the surface energy; a high surface energy results in a larger contact area and stiffness. Murphy et al. (1984) showed that those surface-energy effects are only sizable at relatively low stresses. However, it is not the stress but the contact force that matters, and for clay-sized grains in shales that are orders of magnitude smaller than sandstone grains, significant surface-energy effects are expected even for stresses in the MPa range (i.e. stresses applied in the present experiments) that might explain the observed stiffness changes (Murphy et al., 1984). Obviously, the Hertz-Mindlin model cannot be applied for shales with non-spherical particles but surface-energy

changes would also affect the stiffness of contacts between non-spherical grains. Water adsorption at grain contacts can also explain the observed increase in dispersion with increased water content: as discussed above, the water in between the grains softens the rock. However, the displacement of water molecules during stress variation (an increase in stress results in an increase of the chemical potential of the water in between the grains, making it energetically more favourable for the water to move away from the grain contact) takes time due to viscous forces. The visco-elastic properties of adsorbed (or bound) water at grain contacts is believed to be significantly different from those of free water (Holt and Kolstø, 2017). The characteristic frequency of stiffness dispersion associated with squirt flow is often written as

$$f_c \propto \frac{K}{\eta}\gamma^3 \tag{23}$$

where K is the bulk modulus of the background material, $\eta$ is fluid viscosity and $\gamma$ is the aspect ratio of soft (crack-like) pores. For aspect ratio $10^{-2}$ – $10^{-3}$ and free water viscosity, this gives a transition frequency in the kHz-MHz range, whereas if the water inside the soft pores is bound or adsorbed to the surfaces, the viscosity may be several orders of magnitude higher (Holt and Kolstø, 2017) and shift the transition into the subseismic frequency regime. Liu et al. (1994) argued that the transition frequency for local flow in shale should be in the $10^0$ Hz range, and also pointed out that the Biot critical frequency is of the order $10^{11}$ Hz.

It has also been shown that deformation of the menisci between the gas and the water phase causes energy dissipation and dispersion (Miksis, 1988; Moerig et al., 1996; Johnson, 2001; Pride et al., 2004). Our observation of dispersion of Young's modulus for fully saturated shales (dispersion is actually largest for full saturation compared to partial saturation) suggests, however, that this effect is not the dominant dispersion mechanism.

The discussion above gives only a qualitative account for the observed water-induced stiffness and dispersion variations. In particular, for shales, the dispersion mechanism and its frequency dependence are not fully understood yet. More experimental and theoretical studies are needed for a quantitative description of the observed effects. In the next paragraph, an attempt is made to relate these theoretical concepts to the presented experimental observations.

**Modelling of the fluid-saturation effects by the anisotropic Gassmann model**

Many of the assumptions underlying the Gassmann model (Appendix A) are invalid for shales. Shales are multimineralic, heterogeneous, and mechanically not relaxed even at seismic frequencies as the present dispersion measurements clearly show. Nevertheless, as shown below, the Gassmann model may still be applicable if the rock-frame modulus and the pore-fluid modulus are used as effective parameters, accounting for rock-fluid interaction effects such as adsorption effects, capillary-pressure effects, and dispersion. Here, we have applied the anisotropic Gassmann model (Gassmann, 1951). A two-phase fluid system consisting of water and air was considered. In the partially saturated rocks, $K_f$ is a mixture of the properties of a liquid and a gas filling up the pore space. A frequently used compromise describing the intermediate state of the fluid distribution (between homogenous and patchy saturation) is given by Brie's empirical equation (Brie et al., 1995):

$$K_{f,Brie} = \left(K_{f,liquid} - K_{f,gas}\right)\left(1 - S_{gas}\right)^{e} + K_{f,gas} \quad (24)$$

where e is an adjustable parameter. The bulk modulus and the density of water were equal to $K_{f,water} = 2{,}3\ GPa$ and $\rho_{water} = 1\ g/cm^3$ while the bulk modulus and the density of air were assumed to be $K_{f,air} = 0{,}1\ MPa$ and $\rho_{air} = 0{,}001\ g/cm^3$. Assuming that discussed adsorption effect is the main contributor of the observed softening with the increased RH, Clark et al. (1980)

have shown that the frame moduli decrease nearly linearly with increasing RH. Since for both Mancos shale and Pierre shale, the water saturation changes nearly linearly with RH, we assume a linear relationship between frame modulus and saturation, and use the two parameters of the liner function as fit parameters (independent for Pierre shale and Mancos shale). Also the effective bulk moduli, $K_s$, of the solid phases of Mancos shale and Pierre shale were used as fit parameters within reasonable bounds (based on the XRD data we have identified about 10 main minerals assembling Mancos shale and Pierre shale I, using moduli of those minerals taken from Mavko et al., 2009, we have performed Voigt and Reuss averaging, which gave us the upper and lower limits of $K_s$). Best fits were obtained for , $K_s$ = 30 GPa for Mancos shale and $K_s$ = 24 GPa for Pierre shale I. Using the homogeneous mixing assumption and inserting the Reuss average for the fluid bulk modulus did not fit the experimental data. However, when the effective fluid bulk modulus is calculated assuming Brie's mixing scenario, with a patchiness exponent e = 2.4, a good fit is obtained. Figure 17 illustrates how the modelled fluid-saturation dependence of vertical P- and S-wave velocities, as well as vertical dynamic Young's modulus and Poisson's ratio, compares with the experimental data obtained at 1Hz.

[Figure 17 about here]

Figure 17 shows that the Gassmann model together with the adsorption effects can fairly well reproduce the observed saturation dependency of the vertical moduli at low frequencies (except for high saturations). The predictions are more accurate for Pierre shale, though. Similar conclusion may be drawn for horizontal moduli (Appendix C) however, predictions for horizontal properties are somewhat less accurate. Calculated values differ from experimental data when saturation increase above ~70% (specially visible for vertical Young's modulus and P-wave velocity) indicating that porosity change (during exposure to different RH) and/or

additional fluid flow mechanism should be considered. The use of Brie's approach does not imply that the observed behaviour is caused by patchiness as part of a dispersive mechanism, rather it may be caused by the capillary pressure effects at microscopic scale. This was suggested by Santos et al. (1990) as part of a low-frequency limit Gassmann approach for partially saturated rocks. Papageorgiou et al. (2016) argued that this effect is mimicked by Brie's law. Further work is required to understand the source and nature of the observed dispersion and how to model it.

## CONCLUSIONS

Mancos shale and Pierre shale I were subjected to a series of experiments in which influence of water saturation on seismic dispersion was investigated. Different saturations of the samples were obtained by exposing core plugs to different relative humidity environments. In addition, for Mancos shale, oven-dried samples were measured. Experiments were carried out in an apparatus allowing for combined static-compaction, ultrasonic and dynamic stiffness measurements at seismic frequencies under triaxial stress conditions. Both shales exhibit a large number of similarities in frequency and saturation dependencies of their properties. This is surprising, considering the differences in porosity and mineralogy between the two shales. Experiments confirmed that both Mancos shale and Pierre shale I can be described by TI symmetry and showed that water saturation has a large impact on dynamic stiffnesses, acoustic velocities, and dispersions of both shales. We have observed up to 50% dispersion in vertical Young's modulus, $E_V$, and 26% in vertical P-wave velocity. Increased water saturation causes increase of the seismic dispersion and (assuming that Cole-Cole fit is meaningful for anisotropic rocks) shift of characteristic frequencies towards higher values. Simultaneously, additional water

content causes strong softening of the samples at seismic frequencies. Saturation sensitivity at ultrasonic frequencies is a result of increased dispersion counteracting the softening effect, which leads to more complex behaviour. Poisson's ratio of both shales exhibits rather small dispersion and strongly depends on saturation. P-wave velocity exhibits lowest discrepancy between seismic and ultrasonic measurements in case of either highly saturated or oven-dry samples, the intermediate states shows that increased water contend strongly increases dispersion. We tend to associated observed rock softening effects with water adsorption at grain contacts, which could also explain increase of Poisson's ratio due to reduction of friction. Poroelastic modelling (anisotropic Gassmann) captures the observed phenomena (except for high saturations) after accounting for water weakening through adsorption effects, and fluid modulus stiffening through Brie's mixing law. However, available models cannot fully capture the observed phenomena.

## ACKNOWLEDGMENTS

This publication has been produced with support from the BIGCCS Centre, performed under the Norwegian research program Centres for Environment-friendly Energy Research (FME). The authors acknowledge the following partners for their contributions: ConocoPhillips, Gassco, Shell, Statoil, TOTAL, ENGIE and the Research Council of Norway (193816/S60). The authors would like to acknowledge financial support from The Research Council of Norway, BP Norge, Dong, Engie, Maersk and Total through the KPN-project “Shale Rock Physics: Improved seismic monitoring for increased recovery” at SINTEF Petroleum Research, and the support from the research project "$CO_2$ permeability along fragmented shale interfaces" supported by the Research Council of Norway (255572).

# APPENDICES

## Appendix A: Anisotropic Gassmann model

The anisotropic form of the Gassmann equation was used to model experimental results (Gassmann, 1951):

$$C_{IJ}^{eff} = C_{IJ}^{fr} + \frac{\alpha}{D^*} b_I b_J \tag{A-1}$$

$$b_I = \beta_I - \frac{C_{1I}^{fr} + C_{2I}^{fr} + C_{3I}^{fr}}{3K_s} \tag{A-2}$$

$$\beta_1 = \beta_2 = \beta_3 = 1 \tag{A-3}$$

$$\beta_4 = \beta_5 = \beta_6 = 0 \tag{A-4}$$

$$\frac{1}{\alpha} = \varphi\left(\frac{1}{K_f} - \frac{1}{K_s}\right) \tag{A-5}$$

$$D^* = 1 + \frac{\alpha}{3K_s}(b_1 + b_2 + b_3) \tag{A-6}$$

where index *fr* denotes the properties of the frame, $K_f$ and $K_s$ stands for the bulk modulus of the pore fluid and the solid phase, respectively, and φ indicates the porosity.

## Appendix B: Cole-Cole model

Assuming that the Cole-Cole model may be applied for anisotropic rocks, the Cole-Cole model was used to fit the measured data (Cole and Cole, 1941):

$$E' = E_\infty + \frac{E_0 - E_\infty}{2}\left[1 - \frac{\sinh(1-\alpha)\ln\omega\tau_0}{\cosh(1-\alpha)\ln\omega\tau_0 + \cos\frac{\alpha\pi}{2}}\right] \tag{B-1}$$

$$E'' = \frac{\frac{E_0 - E_\infty}{2}\cos\frac{\alpha\pi}{2}}{\cosh(1-\alpha)\ln\omega\tau_0 + \sin\frac{\alpha\pi}{2}} \tag{B-2}$$

here $E_\infty, E_0$ denote the high- and low- frequency moduli, respectively, $\tau_0$ stand for the relaxation time, $E'$ and $E''$ are a real and an imaginary part of complex modulus, $\omega$ is the angular frequency

and $\alpha$ is a parameter accounting for the width of the relaxation time distribution. The magnitude of the modulus is equal to $\sqrt{E'^2 + E''^2}$ and associated attenuation can be found by $Q_E^{-1} = \frac{E'}{E''}$.

**Appendix C: Modelling of the fluid-saturation effects for horizontal moduli by the anisotropic Gassmann model**

Following the procedure described in the "Modelling of the fluid-saturation effects by the anisotropic Gassmann model" section and keeping values of all the fitting parameters unchanged the horizontal moduli of Mancos shale and Pierre shale I were modelled. Figure C - 1 illustrates how the modelled fluid-saturation dependence of horizontal P- and S-wave velocities, as well as horizontal dynamic Young's modulus and Poisson's ratio, compares with the experimental data obtained at 1Hz.

[Figure C - 1 about here]

**Appendix D: Numerical values of measured and calculated properties of tested shales**

Numerical values of measured and calculated directional Young's moduli and Poisson's ratios, directional P- and S-wave velocities, Thomsen's anisotropy parameters, and independent elements of anisotropy tensor of tested shales at seismic (1 Hz, 21 Hz, 105 Hz) and ultrasonic frequencies, are tabulated below:

[Table D - 1 about here]

[Table D - 2 about here]

[Table D - 3 about here]

[Table D - 4 about here]

[Table D - 5 about here]

[Table D - 6 about here]

[Table D - 7 about here]

[Table D - 8 about here]

[Table D - 9 about here]

[Table D - 10 about here]

[Table D - 11 about here]

## REFERENCES

Batzle, M., R. Hofmann, M. Prasad, G. Kumar, L. Duranti, and D. Han, 2005, Seismic attenuation: observations and mechanisms: SEG Technical Program Expanded Abstracts 2005, SEG, 1565-1568.

Batzle, M., D. Han, and R. Hofmann, 2006, Fluid mobility and frequency-dependent seismic velocity — Direct measurements: Geophysics, **71**, no. 1, N1-N9.

Bauer, A., D. Szewczyk, J. Hedegaard, and R. M. Holt, 2015, Seismic dispersion in Mancos shale: 3rd International Workshop on Rock Physics.

Berryman, J. G., 1988, Seismic wave attenuation in fluid-saturated porous media: Pure and Applied Geophysics, **128**, 423-432.

Biot, M. A., 1956, Theory of propagation of elastic waves in a fluid-saturated porous solid. I. Low-frequency range: The Journal of the Acoustical Society of America, **28**, 168-178.

Brie, A., F. Pampuri, A. F. Marsala, and O. Meazza, 1995, Shear sonic interpretation in gas-bearing sands: 1995 Annual Technical Conference and Exhibition, SPE, Proceedings, 701-710.

Chenevert, M. E., and M. Amanullah, 1997, Shale preservation and testing techniques for borehole stability studies: 1997 SPE/IADC Drilling Conference, SPE/IADC, Proceedings, 863-868.

Clark, V. A., B. R. Tittmann, and T. W. Spencer, 1980, Effect of volatiles on attenuation ($Q^{-1}$) and velocity in sedimentary rocks: Journal of Geophysical Research: Solid Earth, **85**, 5190-5198.

Cole, K. S., and R. H. Cole, 1941, Dispersion and absorption in dielectrics – I. Alternating current characteristics: The Journal of Chemical Physics, **9**, 341–352.

Dell Piane, C., J. Sarout, C. Madonna, E. H. Saenger, D. N. Dewurst, and M. Raven, 2014, Frequency-dependent seismic attenuation in shales: experimental results and theoretical analysis: Geophysical Journal International, **198**, 504-515.

Duranti, L., R. Ewy, and R. Hofmann, 2005, Dispersive and attenuative nature of shales: multiscale and multifrequency observations: SEG Technical Program Expanded Abstracts 2005, SEG, 1577-1580.

Dvorkin, J., and A. Nur, 1993, Dynamic poroelasticity: A unified model with the squirt and the Biot mechanisms: Geophysics, **58**, 524-533.

Gassmann, F., 1951, Elasticity of porous media, in M. A. Pelissier, H. Hoeber, N. van de Coevering, and I. F. Jones, eds., Classics of Elastic Wave Theory: Society of Exploration Geophysicists, 389-408.

Greenspan, L., 1977, Humidity fixed points of binary saturated aqueous solutions: Journal of Research of the National Bureau of Standards, **81**, 89-96.

Helbig, K., 1994, Foundations of Anisotropy for Exploration Seismics: Pergamon Press.

Holt, R. M., O. M. Nes, J. F. Stenebråten, and E. Fjær, 2012, Static vs. dynamic behavior of shale: 46th US Rock Mechanics / Geomechanics Symposium, ARMA, Proceedings, ARMA-2012-542.

Holt, R. M., A. Bauer, F. Fjaer, J. F. Stenebråten, D. Szewczyk, and P. Horsrud, 2015, Relating static and dynamic mechanical anisotropies of shale: 49th U.S. Rock Mechanics/Geomechanics Symposium, ARMA, Proceedings, ARMA-2015-484.

Holt, R. M., and M. I. Kolstø, 2017, How does water near clay mineral surfaces influence the rock physics of shales?: Geophysical Prospecting, in press. Doi: 10.1111/1365-2478.12503.

Hornby, B. E., 1998, Experimental laboratory determination of the dynamic elastic properties of wet, drained shales: Journal of Geophysical Research: Solid Earth, **103**, 29945-29964.

Johnson, D.L., 2001, Theory of frequency dependent acoustics in patchy-saturated porous media: The Journal of the Acoustical Society of America, **110**, 682-694.

Johnson, K. L., K. Kendall, and A. D. Roberts, 1971. Surface energy and the contact of elastic solids: Proceedings of the Royal Society of London A: Mathematical, Physical and Engineering Sciences, **324**, 301-313.

Johnston, D., 1987, Physical properties of shale at temperature and pressure: Geophysics, **52**, 1391-1401.

Johnston, J. E., and N. I. Christensen, 1995, Seismic anisotropy of shales: Journal of Geophysical Research: Solid Earth, **100**, 5991-6003.

Jones, L. E. A., and H. F. Wang, 1981, Ultrasonic velocities in Cretaceous shales from the Williston basin: Geophysics, **46**, 288-297.

Kaarsberg, E. A., 1959, Introductory studies of natural and artificial argillaceous aggregates by sound-propagation and X-ray diffraction methods: The Journal of Geology, **67**, 447-472.

Kellogg, H.E., 1977, Geology and petroleum of the Mancos B formation Douglas Creek Arch area, Colorado and Utah: in Veal, H.K., eds., Exploration frontiers of the central and southern Rockies: Rocky Mountain Association of Geologists, 167–179.

Liu, X., L. Vemik, and A. Nur, 1994, Effects of saturating fluids on seismic velocities in shale: SEG Technical Program Expanded Abstracts 1994, SEG, 1121-1124.

Mavko, G., and A. Nur, 1979, Wave attenuation in partially saturated rocks: Geophysics, **44**, 161-178.

Mavko, G., T. Mukerji, and J. Dvorkin, 2009, The rock physics handbook: Cambridge University Press.

Mikhaltsevitch, V., M. Lebedev, and B. Gurevich, 2016, A laboratory study of the elastic anisotropy in the Mancos shale at seismic frequencies: 86th Annual Meeting, SEG, Technical Program Expanded Abstracts, 3174-3178.

Miksis, M. J., 1988, Effects of contact line movement on the dissipation of waves in partially saturated rocks: Journal of Geophysical Research: Solid Earth, **93**, 6624-6634.

Moerig, R., W. F. Waite, O. S. Boyd, I. C. Getting, and H. A. Spetzler, 1996, Seismic attenuation in artificial glass cracks: Physical and physicochemical effects of fluids: Geophysical Research Letters, **23**, 2053-2056.

Morsy, S., J.J. Sheng, and R. O. Ezewu, 2013, Potential of waterflooding in shale formations: Presented at the 2013 SPE Nigeria Annual International Conference and Exhibition, SPE.

Müller, T. M., B. Gurevich, and M. Lebedev, 2010, Seismic wave attenuation and dispersion resulting from wave-induced flow in porous rocks – a review: Geophysics, **75**, no. 5, 75A147-75A164.

Murphy, W. F., K.W. Winkler, and R.L. Kleinberg, 1984, Frame modulus reduction in sedimentary rocks: the effect of adsorption on grain contacts: Geophysical Research Letters, **11**, 805-808.

Nye, J.F., 1985, Physical properties of crystals: their representation by tensors and matrices: Oxford University Press.

Olgaard, D.L., R. Nuesch, and J. Urai, 1995, Consolidation of water saturated shales at great depth under drained conditions: 8th Congress of the International Society for Rock Mechanics, ISRM, Proceedings, 25-29.

Papageorgiou, G., K. Amalokwu, and M. Chapman, 2016, Theoretical derivation of a Brie-like fluid mixing law: Geophysical Prospecting, **64**, 1048-1053.

Pride, S. R., J. G. Berryman, and J. M. Harris, 2004, Seismic attenuation due to wave-induced flow: Journal of Geophysical Research: Solid Earth, **109**, B01201.

Santos, J.E., J. M. Corberó, and J. Douglas, 1990, Static and dynamic behavior of a porous solid saturated by a two-phase fluid: The Journal of the Acoustical Society of America, **87**, 1428-1438.

Sarker, R. and M. Batzle, 2010, Anisotropic elastic moduli of the Mancos B shale- An experimental study: SEG Technical Program Expanded Abstracts 2010, SEG, 2600-2605.

Schultz, L. G., 1964, Quantitative interpretation of mineralogical composition from X-ray and chemical data for the Pierre Shale: U.S. Geological Survey professional paper, No. 391-C.

Schultz, L. G., H. A. Tourtelot, J. R. Gill, and J. G. Boerngen, 1980, Composition and properties of the Pierre Shale and equivalent rocks, northern Great Plains region: U.S. Geological Survey professional paper, No. 1064-B.

Spencer, J. W., 1981, Stress relaxations at low frequencies in fluid-saturated rocks: attenuation and modulus dispersion: Journal of Geophysical Research: Solid Earth, **86**, 1803-1812.

Suarez-Rivera, R., S. Willson, S. Nakagawa, O. M. Nes, and Z. Liu, 2001, Frequency scaling for evaluation of shale and mudstone properties from acoustic velocities: 2001 AGU Fall Meeting Abstracts, AGU, T32E-0924.

Szewczyk, D., A. Bauer, and R. M. Holt, 2016, A new laboratory apparatus for the measurement of seismic dispersion under deviatoric stress conditions: Geophysical Prospecting, **64**: 789–798.

Szewczyk, D., A. Bauer, and R. M. Holt, 2017, Stress dependent elastic properties of shales – Laboratory experiments at seismic and ultrasonic frequencies: Geophysical Journal International – in press.

Tarantino, A., 2010, Basic concepts in the mechanics and hydraulics of unsaturated geomaterials, in L. Laloui, eds., Mechanics of unsaturated geomaterials: ISTE Ltd.

Thomsen, L., 1986, Weak elastic anisotropy: Geophysics, **51**, 1954-1966.

Torsaeter, M., P. E. Vullum, and O. M. Nes, 2012, Nanostructure vs. macroscopic properties of Mancos Shale: 2012 SPE Canadian Unconventional Resources Conference, SPE, SPE-162737.

Vales, F., D. Nguyen Minha, H. Gharbia, and A. Rejebb, 2004, Experimental study of the influence of the degree of saturation on physical and mechanical properties in Tournemire shale (France): Applied Clay Science, **26**, 197-207.

Vernik, L. and A. Nur, 1992, Ultrasonic velocity and anisotropy of hydrocarbon source rocks: Geophysics, **57**, 727-735.

Voigt, W., 1928, Lehrbuch der Kristallphysik (mit Ausschluss der Kristalloptik), B.G. Teubner.

Wang, Z., 2002, Seismic anisotropy in sedimentary rocks, part 2: Laboratory data: Geophysics, **67**, 1423-1440.

White, J. E., N. Mihailova, and F. Lyakhovitsky, 1975, Low-frequency seismic waves in fluid-saturated layered rocks: The Journal of the Acoustical Society of America, **57**, S30.

Winkler, K., and A. Nur, 1979, Pore fluids and seismic attenuation in rocks: Geophysical Research Letters, **6**, 1-4.

Yurikov, A., M. Lebedev, and M. Pervukhina, 2017, Water retention effects on the elastic properties of Opalinus shale: Presented at 4th International Workshop on Rock Physics.

LIST OF FIGURES

Figure 1 – Mass change of Mancos shale and Pierre shale I core plugs used during experiments. In order to achieve various saturation levels, as-received core plugs were placed in the desiccators with various relative humidity (RH) and were stabilizing under room temperature.

Figure 2 - Schematic drawings of the experimental setup (a) and the sample with attached strain (b). Indicated on the drawings are: piston (A), pressure vessel (B), linear variable displacement transducer (LVDT), measuring axial quasi-static deformations (C), adapter plates holding the LVDTs (D), aluminum standard with attached strain gages for phase shift measurements (E), piezoelectric force sensor, measuring force modulations at seismic frequencies (F), piezoelectric actuator, generating displacement modulations at seismic frequencies (G), internal load cell, measuring quasi-static deviatoric stress (H), top and bottom endcaps with embedded compressional and shear wave transducers and pore-fluid lines (I), sample (J), strain gages attached to sample (K), rubber sleeve around the sample that seals the sample from the oil in the cell used for applying confining stress (L), and pore-fluid lines (M).

Figure 3 - Directly measured anisotropic properties obtained with three differently oriented Mancos shale core plugs for RH = 12 % and RH = 86 %. (a-d) directional Young's moduli and Poisson's ratios measured at seismic frequencies. (e) directional P- and S-wave velocities measured at ultrasonic frequencies. (f) Seismic $(E_H/E_V)/(\nu_{HV}/\nu_{VH})$, that for TI symmetry should be equal to 1, measured for both saturations.

Figure 4 – Directly measured anisotropic properties obtained with three differently oriented Pierre shale I core plugs for RH = 19 % and RH = 55 %. (a-d) directional Young's moduli and Poisson's ratios measured at seismic frequencies. (e) directional P- and S-wave velocities

measured at ultrasonic frequencies. (f) Seismic $(E_H/E_V)/(\nu_{HV}/\nu_{VH})$, that for TI symmetry should be equal to 1, measured for both saturations.

Figure 5 – Directly measured saturation dependence of seismic vertical Young's modulus (a) and Poisson's ratio (b), as well as ultrasonic P- and S-wave velocities (c) of partially saturated Mancos shale.

Figure 6 – Directly measured saturation dependence of seismic vertical Young's modulus (a) and Poisson's ratio (b), as well as ultrasonic P- and S-wave velocities (c) of partially saturated Pierre shale I.

Figure 7 – Sensitivity of conversion from measured ultrasonic velocities to vertical Young's modulus (a), Poisson's ratio (b), and sensitivity of conversion from measured seismic engineering parameters to vertical S-wave velocity (c) of Mancos shale to the errors in determination of sample-orientation, as well as images of $0^o$, $45^o$, and $90^o$ oriented Mancos shale core plugs (d). Ultrasonic points (a,b) or seismic points (c) were calculated with the use of measured velocities/engineering parameters of samples cut under angles of $0^o$, $45^o$, and $90^o$ with respect to the bedding. While keeping the measured values constant we have allowed for variations ($\pm 10^o$) to the bedding angle of samples drilled at $45^o$.

Figure 8 – Sensitivity of conversion from measured ultrasonic velocities to vertical Young's modulus (a), and Poisson's ratio (b), as well as sensitivity of conversion from measured seismic engineering parameters to vertical S-wave velocity (c), of Pierre shale I to the errors in determination of sample-orientation. Ultrasonic points (a,b) or seismic points (c) were calculated with the use of measured velocities/engineering parameters of samples cut under angles $0^o$, $45^o$, and $90^o$ with respect to the bedding. While keeping the measured values constant we have allowed for variations ($\pm 10^o$) to the bedding angle of samples drilled at $45^o$.

Figure 9 – Velocity anisotropy (Thomsen's parameters) obtained with three differently oriented Mancos shale core plugs (for RH = 12 % and RH = 86 %) and Pierre shale core plugs (for RH = 19 % and RH = 55 %).

Figure 10 – Seismic and ultrasonic independent stiffness parameters, $C_{ij}$'s, obtained with three differently oriented Mancos shale core plugs (for RH = 12 % and RH = 86 %) and Pierre shale core plugs (for RH = 19 % and RH = 55 %).

Figure 11 - Stiffness parameters, $C_{ij}$'s, determined at seismic and ultrasonic frequencies for the remaining partially saturated Mancos shale samples. Data were calculated from measurements performed with $0^O$-oriented samples by assuming extrapolated Thomsen's parameters.

Figure 12 - Stiffness parameters, $C_{ij}$'s, determined at seismic and ultrasonic frequencies for the remaining partially saturated Pierre shale samples. Data were calculated from measurements performed with $0^O$-oriented samples by assuming extrapolated Thomsen's parameters.

Figure 13 – Saturation dependence of vertical Young's modulus, $E_V$, and Poisson's ratio, $\nu_{VH}$, of Mancos shale as a function of frequency. Seismic points were measured directly while ultrasonic points were calculated from ultrasonic velocities. Solid and dashed lines in (a) show manual Cole-Cole fits to the experimental data (Cole and Cole 1941).

Figure 14 – Saturation dependence of vertical Young's modulus, $E_V$, and Poisson's ratio, $\nu_{VH}$, of Pierre shale I as a function of frequency. Seismic points were measured directly while ultrasonic points were calculated from ultrasonic velocities. Solid and dashed lines in (a) show manual Cole-Cole fits to the experimental data (Cole and Cole 1941).

Figure 15 – Vertical P- and S-wave velocities of partially saturated Mancos shale as a function of saturation for seismic and ultrasonic frequencies. Ultrasonic points were measured directly while

velocities at seismic frequencies were calculated from measured seismic Young's moduli and Poisson's ratios with the use of densities of tested core plugs.

Figure 16 – Vertical P- and S-wave velocities of partially saturated Pierre shale as a function of saturation for seismic and ultrasonic frequencies. Ultrasonic points were measured directly while velocities at seismic frequencies were calculated from measured seismic Young's moduli and Poisson's ratios with the use of densities of tested core plugs.

Figure 17 – Comparison of measured vertical properties of Mancos shale and Pierre shale with the anisotropic Gassmann model: (a-d) P- and S-wave velocities; (e,f) Young's moduli, $E_V$; (g,h) Poisson's ratio, $\nu_{VH}$. Experimentally measured frame moduli (Mancos – RH = 12%, Pierre shale – RH = 19%) were assumed to change linearly with water saturation and effective fluid modulus was calculated according to Brie's mixing scenario.

Figure C - 1 – Comparison of measured horizontal properties of Mancos shale and Pierre shale with the anisotropic Gassmann model: (a-d) P- and S-wave velocities; (e,f) Young's moduli, $E_H$; (g,h) Poisson's ratio, $\nu_{HV}$. Experimentally measured frame moduli (Mancos – RH = 12%, Pierre shale – RH = 19%) were assumed to change linearly with water saturation and effective fluid modulus was calculated according to Brie's mixing scenario.

LIST OF TABLES

elements of anisotropy tensor of Mancos shale RH=76% at seismic (1 Hz, 21 Hz, 105 Hz) and ultrasonic frequencies.

Table D - 6. List of measured and calculated directional Young's moduli and Poisson's ratios, directional P- and S-wave velocities, Thomsen's anisotropy parameters, and independent elements of anisotropy tensor of as-received Mancos shale at seismic (1 Hz, 21 Hz, 105 Hz) and ultrasonic frequencies.

Table D - 7. List of measured and calculated directional Young's moduli and Poisson's ratios, directional P- and S-wave velocities, Thomsen's anisotropy parameters, and independent elements of anisotropy tensor of Mancos shale RH=100% at seismic (1 Hz, 21 Hz, 105 Hz) and ultrasonic frequencies.

Table D - 8. List of measured and calculated directional Young's moduli and Poisson's ratios, directional P- and S-wave velocities, Thomsen's anisotropy parameters, and independent elements of anisotropy tensor of Pierre shale RH=19% at seismic (1 Hz, 21 Hz, 105 Hz) and ultrasonic frequencies.

Table D - 9. List of measured and calculated directional Young's moduli and Poisson's ratios, directional P- and S-wave velocities, Thomsen's anisotropy parameters, and independent elements of anisotropy tensor of Pierre shale RH=34% at seismic (1 Hz, 21 Hz, 105 Hz) and ultrasonic frequencies.

Table D - 10. List of measured and calculated directional Young's moduli and Poisson's ratios, directional P- and S-wave velocities, Thomsen's anisotropy parameters, and independent elements of anisotropy tensor of Pierre shale RH=55% at seismic (1 Hz, 21 Hz, 105 Hz) and ultrasonic frequencies.

Table D - 11. List of measured and calculated directional Young's moduli and Poisson's ratios, directional P- and S-wave velocities, Thomsen's anisotropy parameters, and independent elements of anisotropy tensor of Pierre shale RH=76% at seismic (1 Hz, 21 Hz, 105 Hz) and ultrasonic frequencies.

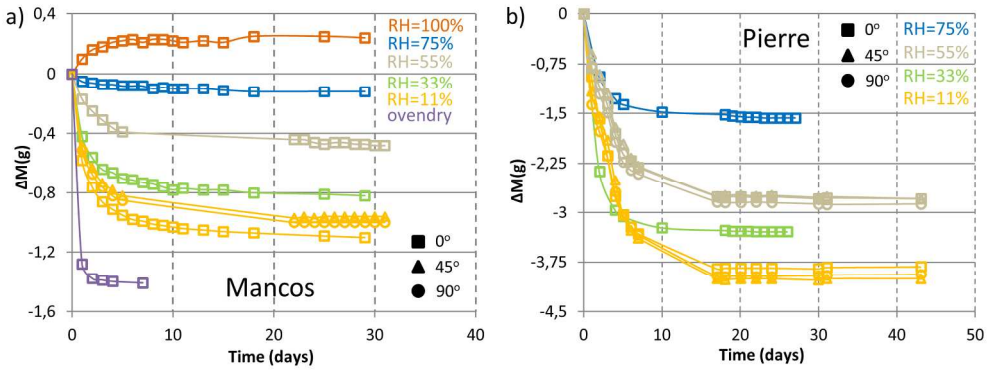


Figure 1 – Mass change of Mancos shale and Pierre shale I core plugs used during experiments. In order to achieve various saturation levels, as-received core plugs were placed in the desiccators with various relative humidity (RH) and were stabilizing under room temperature.

200x75mm (300 x 300 DPI)

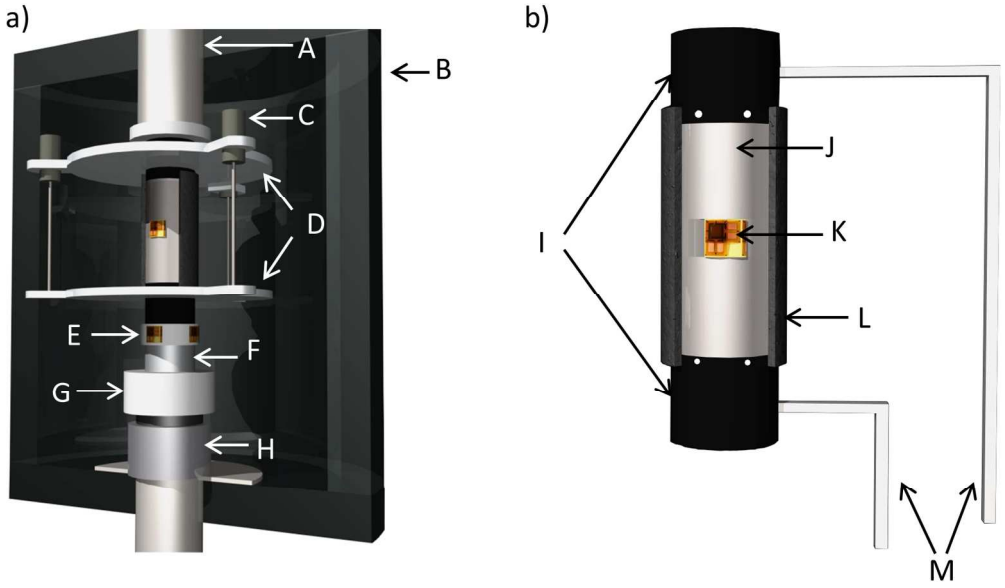


Figure 2 - Schematic drawings of the experimental setup (a) and the sample with attached strain gages (b). Indicated on the drawings are: piston (A), pressure vessel (B), linear variable displacement transducer (LVDT), measuring axial quasi-static deformations (C), adapter plates holding the LVDTs (D), aluminum standard with attached strain gages for phase shift measurements (E), piezoelectric force sensor, measuring force modulations at seismic frequencies (F), piezoelectric actuator, generating displacement modulations at seismic frequencies (G), internal load cell, measuring quasi-static deviatoric stress (H), top and bottom endcaps with embedded compressional and shear wave transducers and pore-fluid lines (I), sample (J), strain gages attached to sample (K), rubber sleeve around the sample that seals the sample from the oil in the cell used for applying confining stress (L), and pore-fluid lines (M).

155x90mm (300 x 300 DPI)

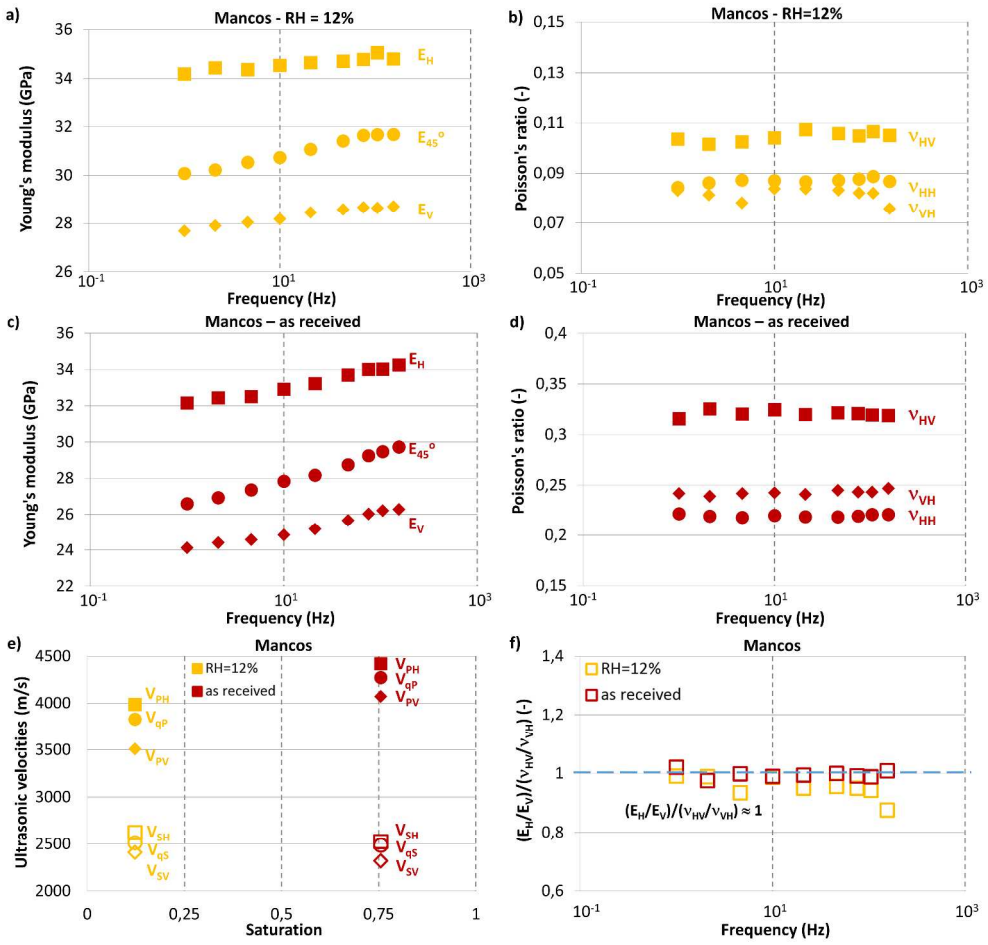


Figure 3 - Directly measured anisotropic properties obtained with three differently oriented Mancos shale core plugs for RH = 12 % and RH = 86 %. (a-d) directional Young's moduli and Poisson's ratios measured at seismic frequencies. (e) directional P- and S-wave velocities measured at ultrasonic frequencies. (f) Seismic $(E_H/E_V)/(\nu_{HV}/\nu_{VH})$, that for TI symmetry should be equal to 1, measured for both saturations.

479x450mm (300 x 300 DPI)

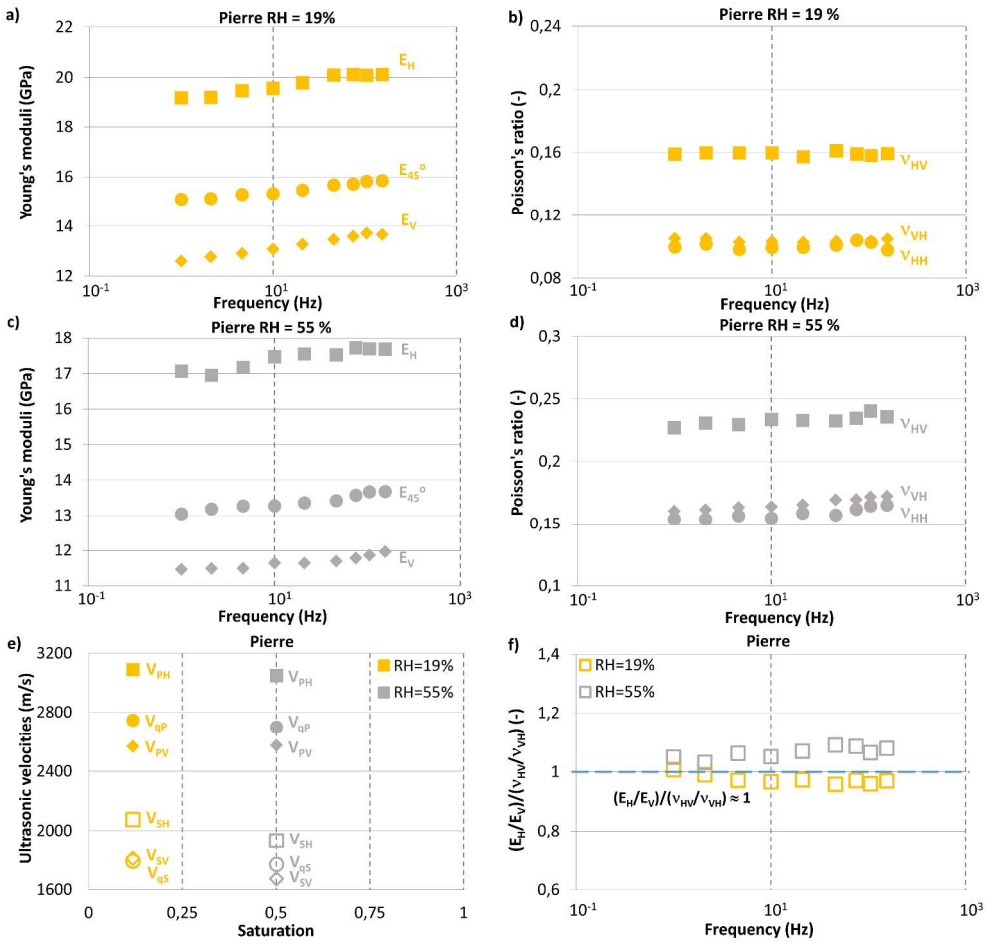


Figure 4 – Directly measured anisotropic properties obtained with three differently oriented Pierre shale I core plugs for RH = 19 % and RH = 55 %. (a-d) directional Young's moduli and Poisson's ratios measured at seismic frequencies. (e) directional P- and S-wave velocities measured at ultrasonic frequencies. (f) Seismic $(E_H/E_V)/(v_{HV}/v_{VH})$, that for TI symmetry should be equal to 1, measured for both saturations.

479x450mm (300 x 300 DPI)

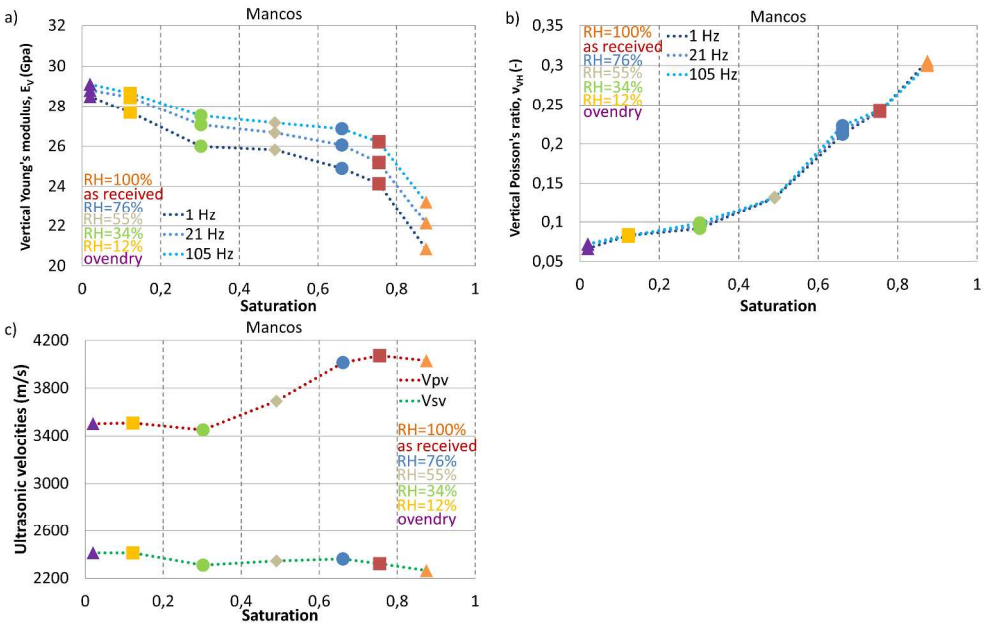


Figure 5 – Directly measured saturation dependence of seismic vertical Young's modulus (a) and Poisson's ratio (b), as well as ultrasonic P- and S-wave velocities (c) of partially saturated Mancos shale.

480x300mm (300 x 300 DPI)

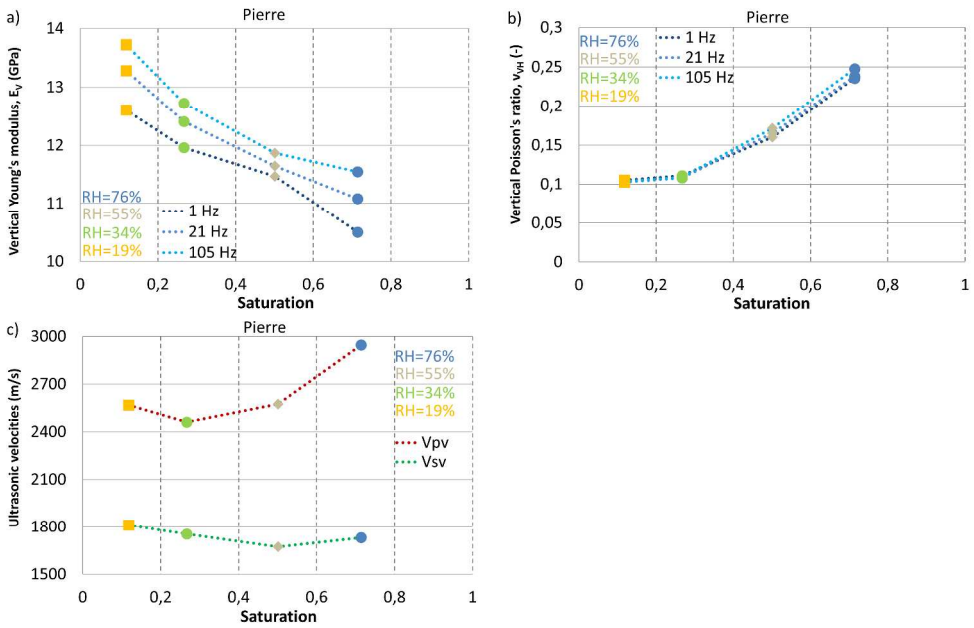


Figure 6 – Directly measured saturation dependence of seismic vertical Young's modulus (a) and Poisson's ratio (b), as well as ultrasonic P- and S-wave velocities (c) of partially saturated Pierre shale I.

480x300mm (300 x 300 DPI)

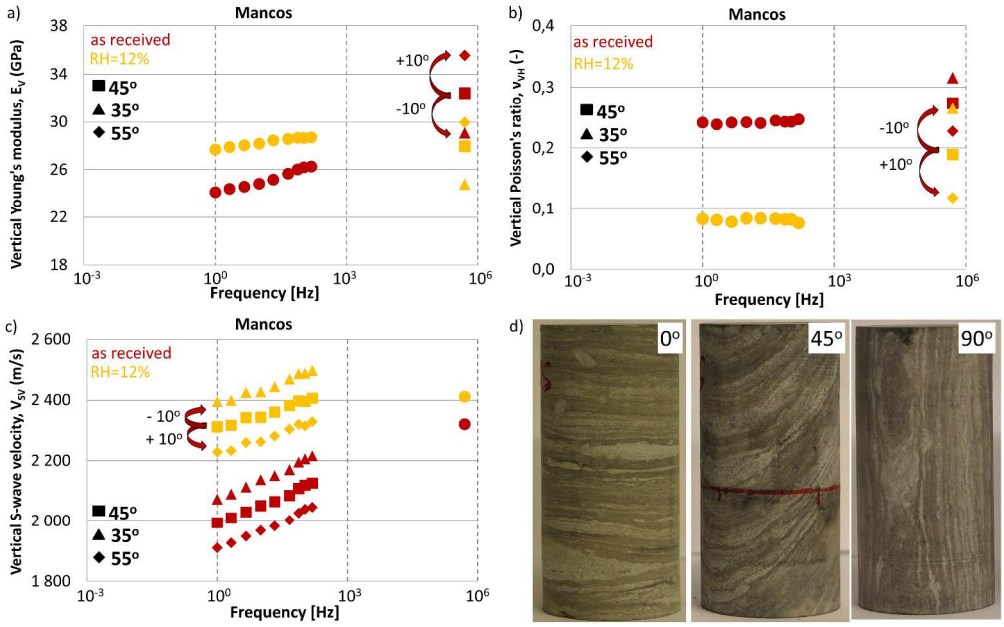


Figure 7 – Sensitivity of conversion from measured ultrasonic velocities to vertical Young's modulus (a), Poisson's ratio (b), and sensitivity of conversion from measured seismic engineering parameters to vertical S-wave velocity (c) of Mancos shale to the errors in determination of sample-orientation, as well as images of 0°, 45°, and 90° oriented Mancos shale core plugs (d). Ultrasonic points (a,b) or seismic points (c) were calculated with the use of measured velocities/engineering parameters of samples cut under angles of 0°, 45°, and 90° with respect to the bedding. While keeping the measured values constant we have allowed for variations (±10°) to the bedding angle of samples drilled at 45°.

480x300mm (300 x 300 DPI)

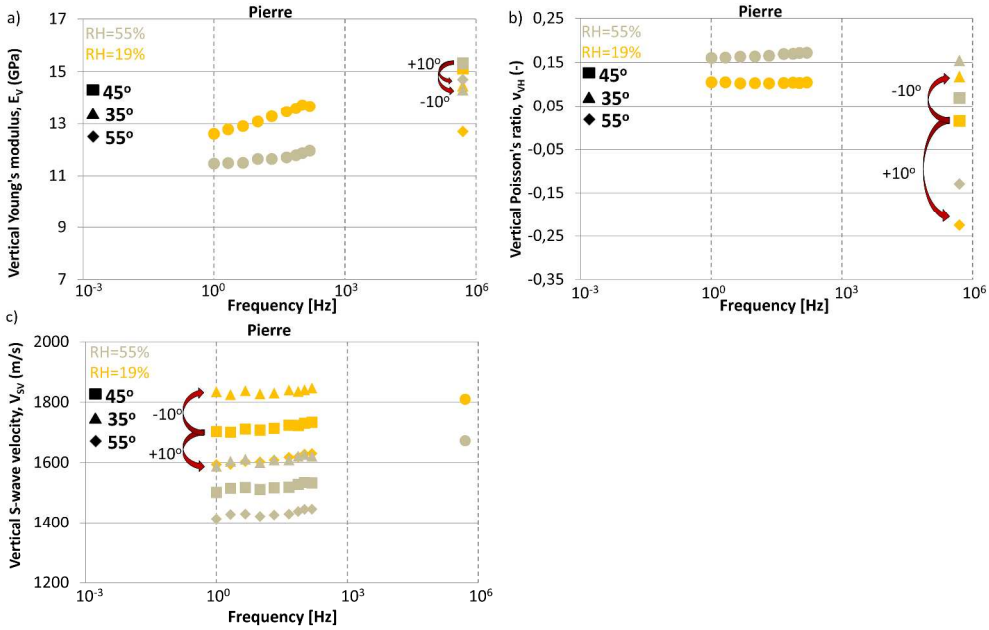


Figure 8 – Sensitivity of conversion from measured ultrasonic velocities to vertical Young's modulus (a), and Poisson's ratio (b), as well as sensitivity of conversion from measured seismic engineering parameters to vertical S-wave velocity (c), of Pierre shale I to the errors in determination of sample-orientation. Ultrasonic points (a,b) or seismic points (c) were calculated with the use of measured velocities/engineering parameters of samples cut under angles 0°, 45°, and 90° with respect to the bedding. While keeping the measured values constant we have allowed for variations (±10°) to the bedding angle of samples drilled at 45°.

480x300mm (300 x 300 DPI)

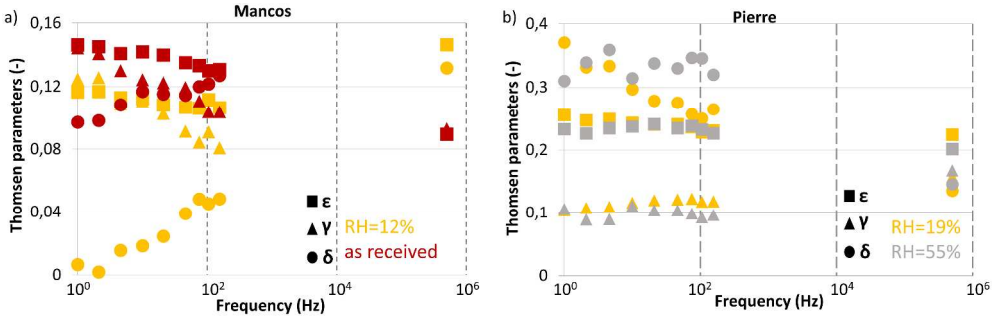


Figure 9 – Velocity anisotropy (Thomsen's parameters) obtained with three differently oriented Mancos shale core plugs (for RH = 12 % and RH = 86 %) and Pierre shale core plugs (for RH = 19 % and RH = 55 %).

479x150mm (300 x 300 DPI)

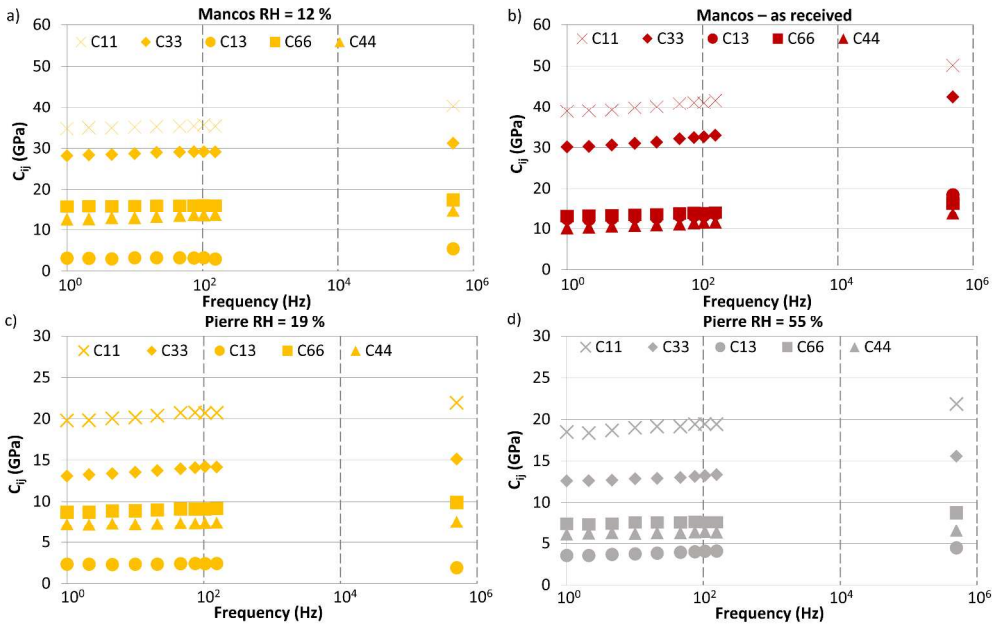


Figure 10 – Seismic and ultrasonic independent stiffness parameters, $C_{ij}$'s, obtained with three differently oriented Mancos shale core plugs (for RH = 12 % and RH = 86 %) and Pierre shale core plugs (for RH = 19 % and RH = 55 %).

479x299mm (300 x 300 DPI)

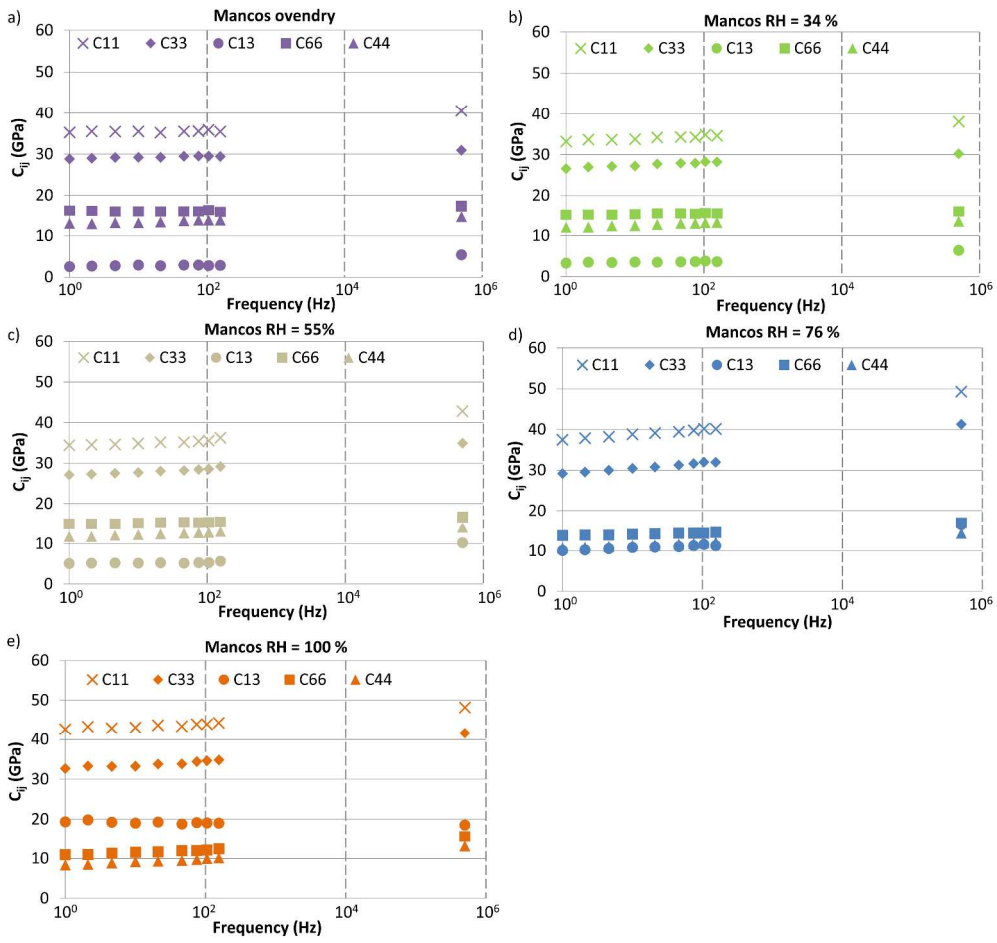


Figure 11 - Stiffness parameters, $C_{ij}$'s, determined at seismic and ultrasonic frequencies for the remaining partially saturated Mancos shale samples. Data were calculated from measurements performed with 0°-oriented samples by assuming extrapolated Thomsen's parameters.

479x450mm (300 x 300 DPI)

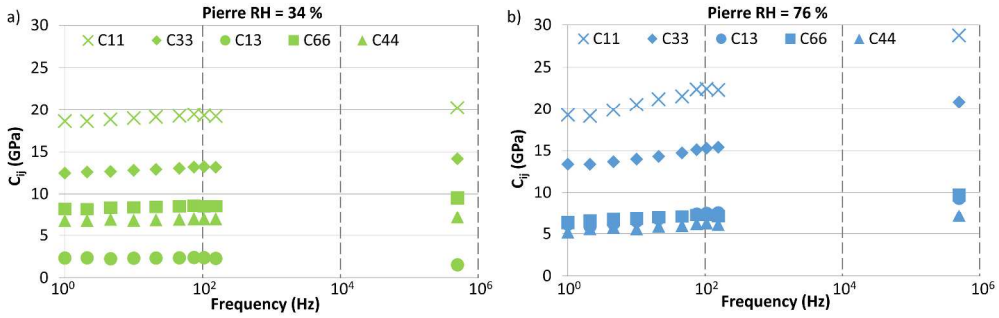


Figure 12 - Stiffness parameters, $C_{ij}$'s, determined at seismic and ultrasonic frequencies for the remaining partially saturated Pierre shale samples. Data were calculated from measurements performed with $0^{o}$-oriented samples by assuming extrapolated Thomsen's parameters.

479x150mm (300 x 300 DPI)

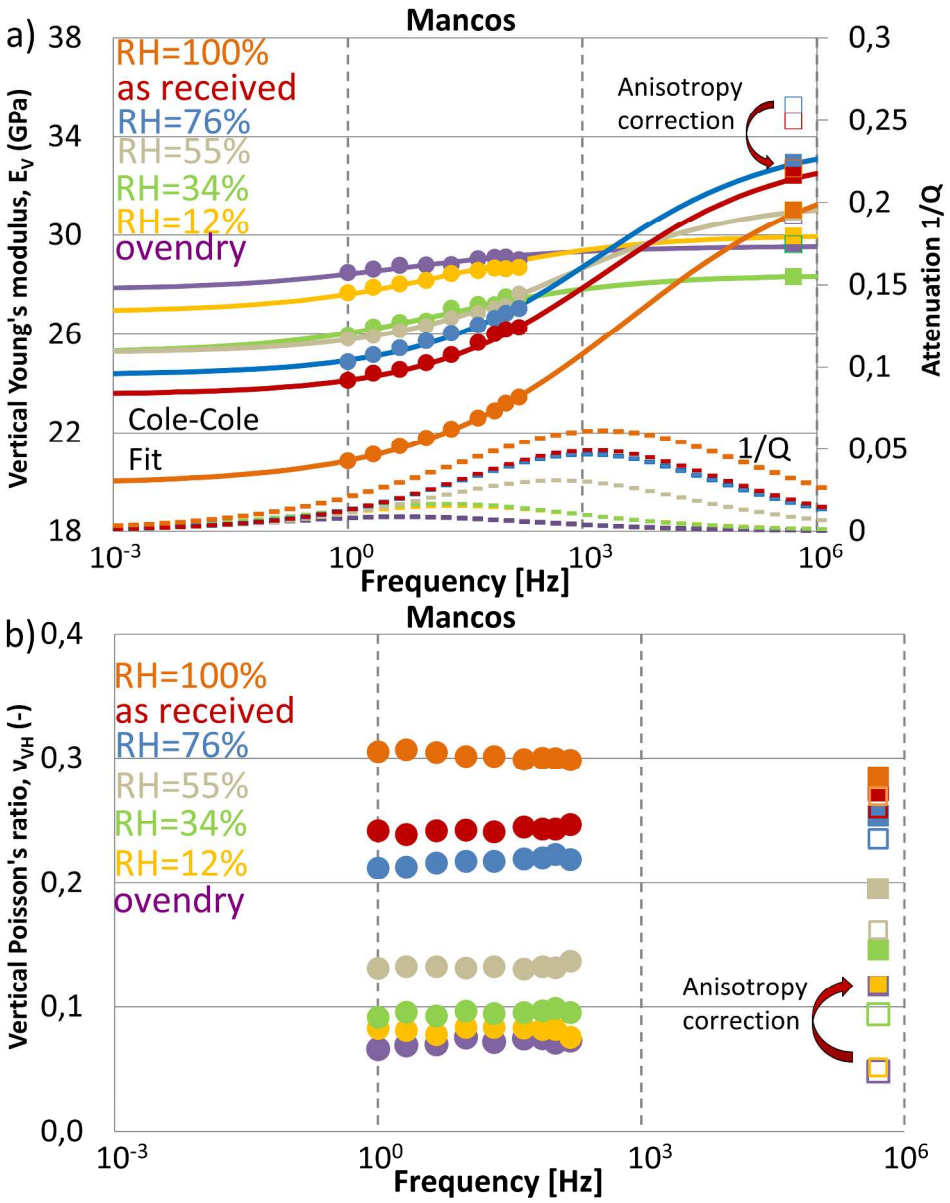


Figure 13 – Saturation dependence of vertical Young's modulus, $E_V$, and Poisson's ratio, $v_{VH}$, of Mancos shale as a function of frequency. Seismic points were measured directly while ultrasonic points were calculated from ultrasonic velocities. Solid and dashed lines in (a) show manual Cole-Cole fits to the experimental data (Cole and Cole 1941).

240x299mm (300 x 300 DPI)

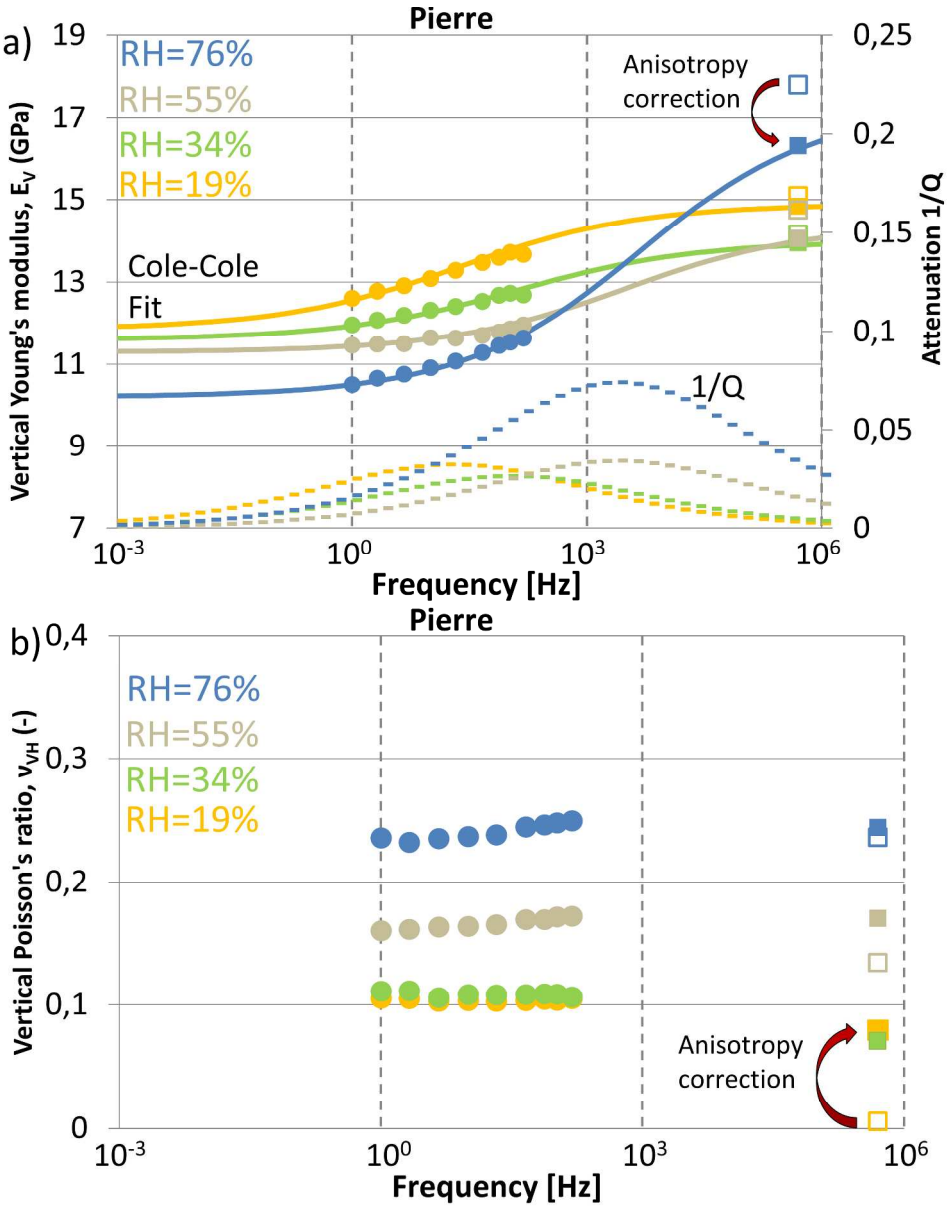


Figure 14 – Saturation dependence of vertical Young's modulus, $E_V$, and Poisson's ratio, $v_{VH}$, of Pierre shale I as a function of frequency. Seismic points were measured directly while ultrasonic points were calculated from ultrasonic velocities. Solid and dashed lines in (a) show manual Cole-Cole fits to the experimental data (Cole and Cole 1941).

240x299mm (300 x 300 DPI)

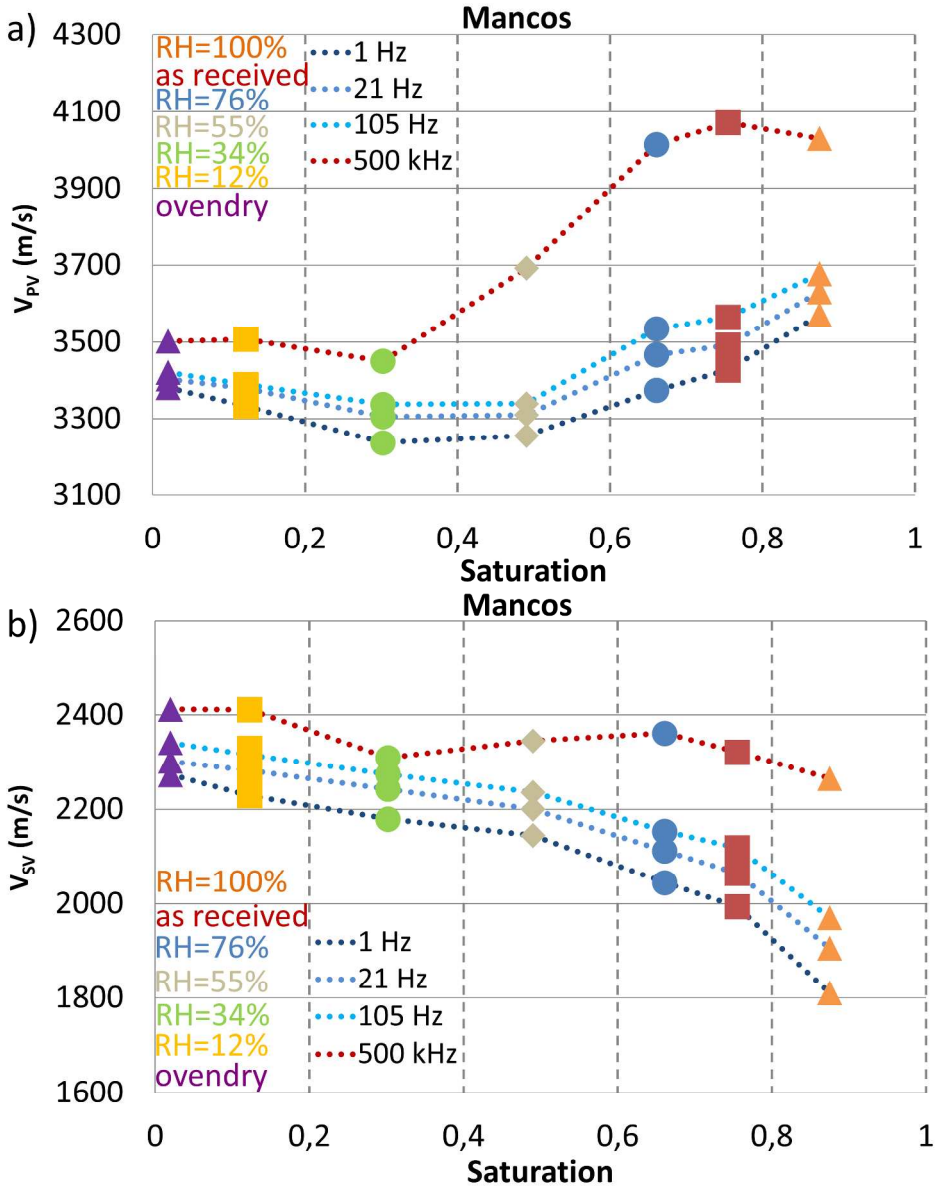


Figure 15 – Vertical P- and S-wave velocities of partially saturated Mancos shale as a function of saturation for seismic and ultrasonic frequencies. Ultrasonic points were measured directly while velocities at seismic frequencies were calculated from measured seismic Young's moduli and Poisson's ratios with the use of densities of tested core plugs.

240x299mm (300 x 300 DPI)

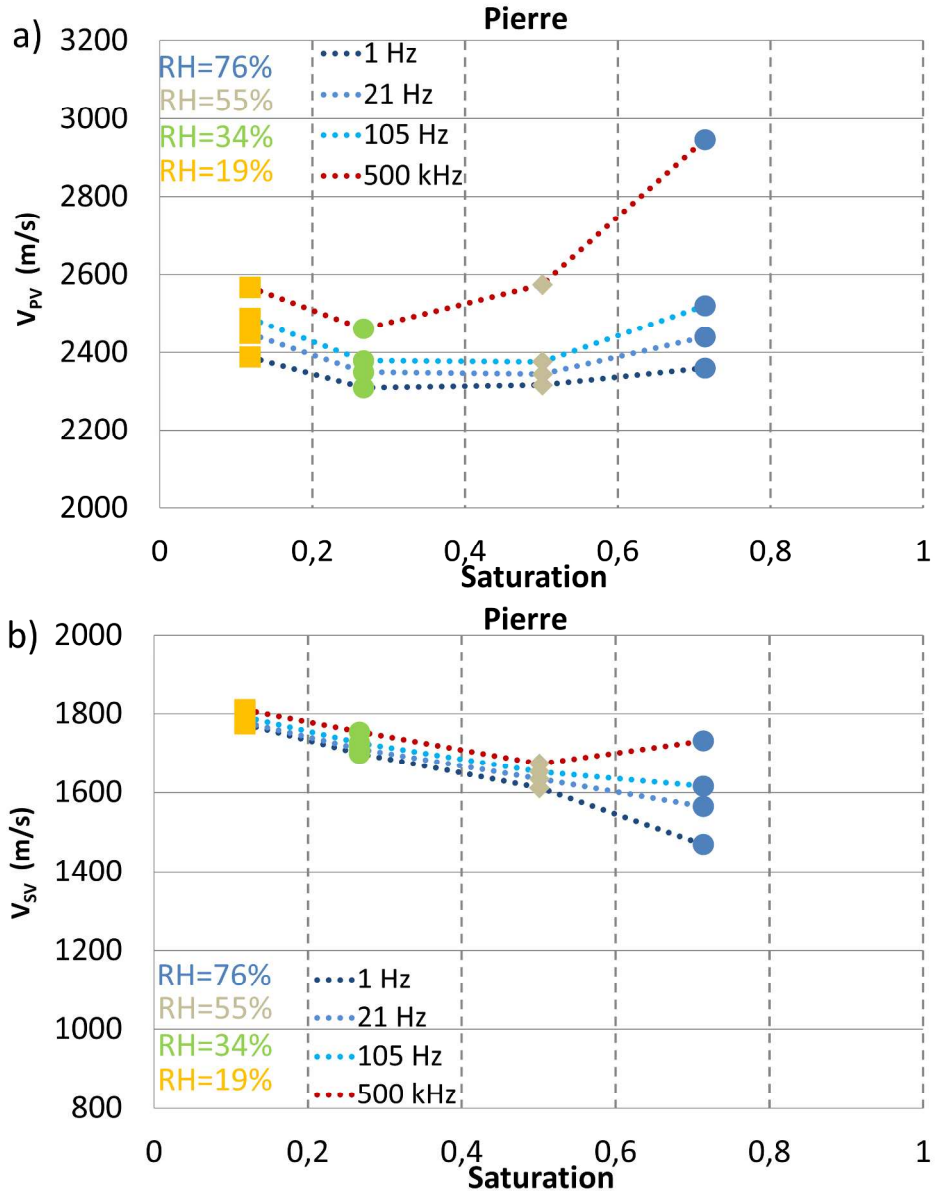


Figure 16 – Vertical P- and S-wave velocities of partially saturated Pierre shale as a function of saturation for seismic and ultrasonic frequencies. Ultrasonic points were measured directly while velocities at seismic frequencies were calculated from measured seismic Young's moduli and Poisson's ratios with the use of densities of tested core plugs.

240x299mm (300 x 300 DPI)

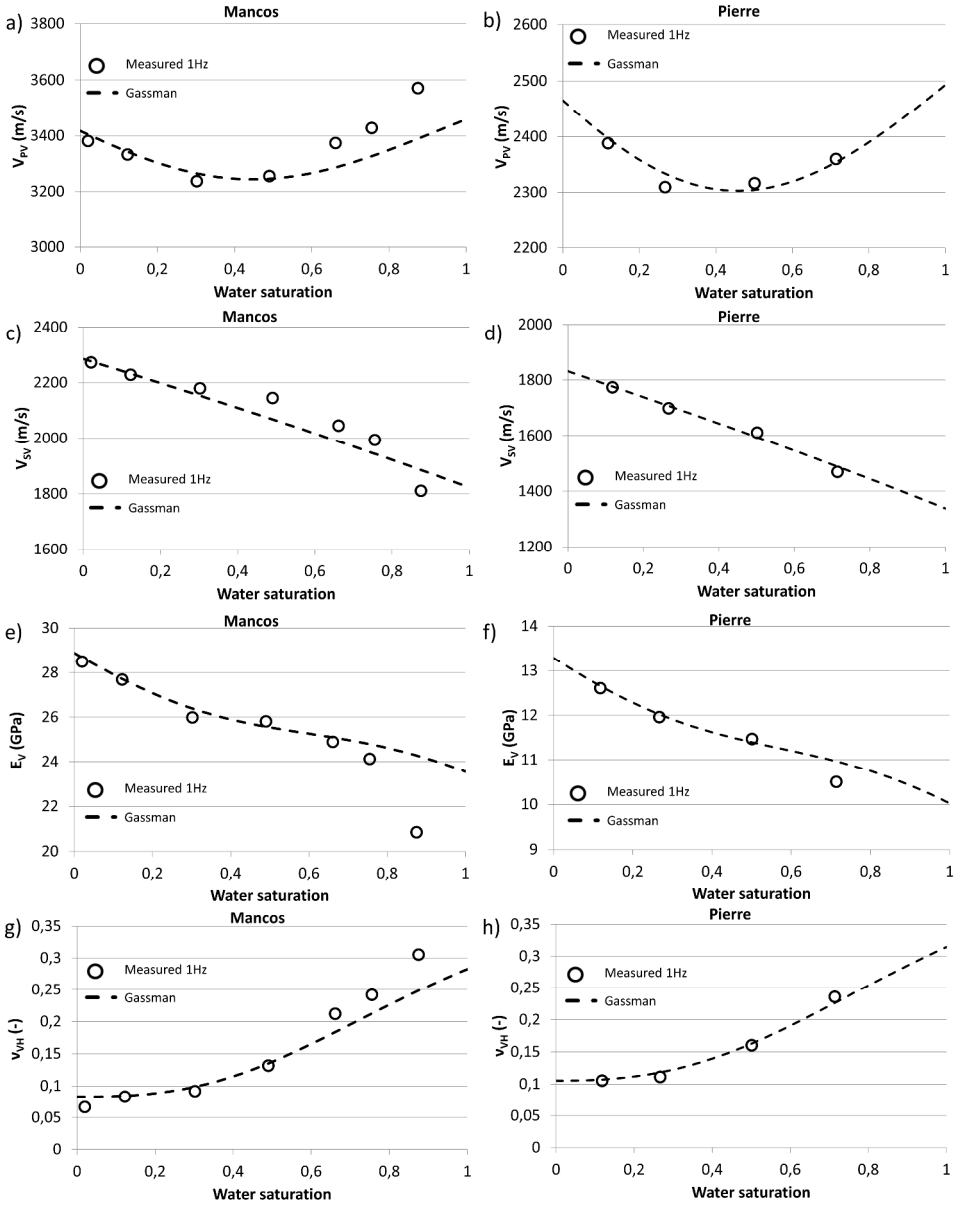


Figure 17 – Comparison of measured vertical properties of Mancos shale and Pierre shale with the anisotropic Gassmann model: (a-d) P- and S-wave velocities; (e,f) Young's moduli, $E_V$; (g,h) Poisson's ratio, $\nu_{VH}$. Experimentally measured frame moduli (Mancos – RH = 12%, Pierre shale – RH = 19%) were assumed to change linearly with water saturation and effective fluid modulus was calculated according to Brie's mixing scenario.

480x600mm (300 x 300 DPI)

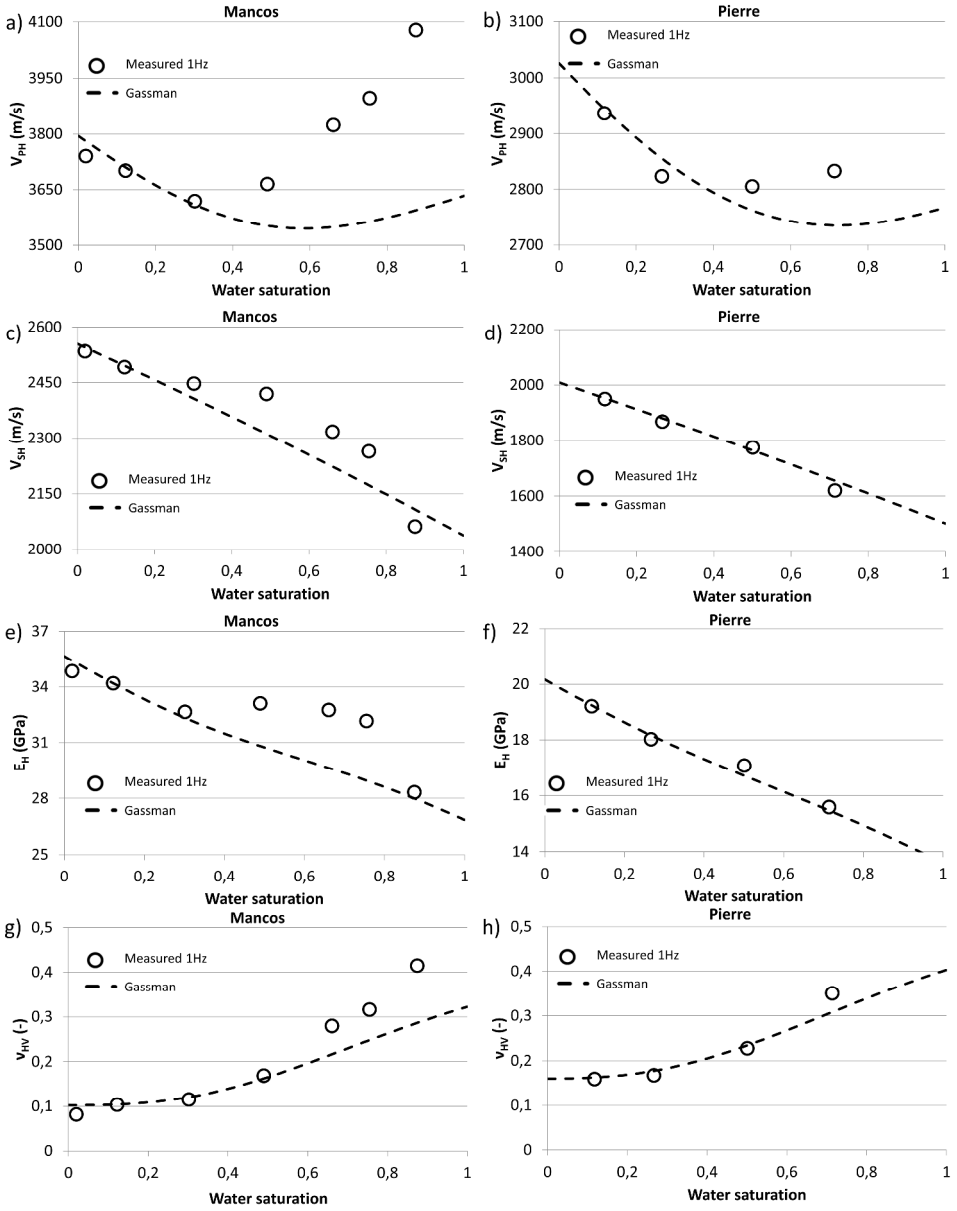


Figure C - 1 – Comparison of measured horizontal properties of Mancos shale and Pierre shale with the anisotropic Gassmann model: (a-d) P- and S-wave velocities; (e,f) Young's moduli, $E_H$; (g,h) Poisson's ratio, $\nu_{HV}$. Experimentally measured frame moduli (Mancos – RH = 12%, Pierre shale – RH = 19%) were assumed to change linearly with water saturation and effective fluid modulus was calculated according to Brie's mixing scenario.

480x600mm (300 x 300 DPI)

Table 1 – List of and orientation of samples used in the experiments, stress states for given experiment, saturant used for RH control during stabilization in desiccators, corresponding relative humidity and saturation of the sample as well as change of the volume of samples during stabilization.

| # of sample | Shale | Orientation with respect to bedding | Saturant used for RH control | RH theoretical (RH measured) | Saturation | Change of volume during stabilization (%) |
|---|---|---|---|---|---|---|
| S 01 | Mancos | $0^{o}$ | Ovendry ($105^{o}$C) | 0% | 0.02 | -0,38 |
| S 02 | Mancos | $0^{o}$ | LiCl | 11.3% (12.2%) | 0.11±0.02 | -0,23 |
| S 03 | Mancos | ~$45^{o}$ | LiCl | 11.3% (12.2%) | 0.11±0.02 | -0,28 |
| S 04 | Mancos | $90^{o}$ | LiCl | 11.3% (12.2%) | 0.11±0.02 | -0,16 |
| S 05 | Mancos | $0^{o}$ | $MgCl_2$ | 32.9% (33.6%) | 0.29±0.03 | -0,12 |
| S 06 | Mancos | $0^{o}$ | $Mg(NO_3)_2$ | 54.4% (54.9%) | 0.47±0.05 | -0,22 |
| S 07 | Mancos | $0^{o}$ | NaCl | 75.4% (75.8%) | 0.63±0.05 | -0,09 |
| S 08 | Mancos | $0^{o}$ | as received | - | 0.72±0.05 | 0 |
| S 09 | Mancos | ~$45^{o}$ | as received | - | 0.72±0.05 | 0 |
| S 10 | Mancos | $90^{o}$ | as received | - | 0.72±0.05 | 0 |
| S 11 | Mancos | $0^{o}$ | pure water | 100% (99.9%) | 0.83±0.06 | 0,31 |
| S 12 | Pierre I | $0^{o}$ | LiCl | 11.3% (18.9%) | 0.10±0.06 | -3,59 |
| S 13 | Pierre I | ~$45^{o}$ | LiCl | 11.3% (18.9%) | 0.10±0.06 | -4,34 |
| S 14 | Pierre I | $90^{o}$ | LiCl | 11.3% (18.9%) | 0.10±0.06 | -3,13 |
| S 15 | Pierre I | $0^{o}$ | $MgCl_2$ | 32.9% (33.9%) | 0.23±0.05 | -3,10 |
| S 16 | Pierre I | $0^{o}$ | $Mg(NO_3)_2$ | 54.4% (55.1%) | 0.48±0.04 | -3,18 |
| S 17 | Pierre I | ~$45^{o}$ | $Mg(NO_3)_2$ | 54.4% (55.1%) | 0.48±0.04 | -2,42 |
| S 18 | Pierre I | $90^{o}$ | $Mg(NO_3)_2$ | 54.4% (55.1%) | 0.48±0.04 | -5,79 |
| S 19 | Pierre I | $0^{o}$ | NaCl | 75.4% (76%) | 0.70±0.02 | -3,16 |

Table D - 1. List of measured and calculated directional Young's moduli and Poisson's ratios, directional P- and S-wave velocities, Thomsen's anisotropy parameters, and independent elements of anisotropy tensor of oven-dry Mancos shale at seismic (1 Hz, 21 Hz, 105 Hz) and ultrasonic frequencies.

| | 1 (Hz) | 21 (Hz) | 105 (Hz) | ultrasonic |
|---|---|---|---|---|
| $E_V$ (GPa) | 28,50 | 28,81 | 29,11 | 29,67 |
| $E_H$ (GPa) | 34,85 | 34,72 | 35,39 | 39,02 |
| $\nu_{VH}$ (-) | 0,067 | 0,072 | 0,072 | 0,117 |
| $\nu_{HV}$ (-) | 0,081 | 0,087 | 0,087 | 0,154 |
| $\nu_{HH}$ (-) | 0,076 | 0,084 | 0,087 | 0,122 |
| $V_{PV}$ (m/s) | 3381 | 3403 | 3421 | 3502 |
| $V_{PH}$ (m/s) | 3740 | 3738 | 3774 | 4010 |
| $V_{SV}$ (m/s) | 2273 | 2301 | 2341 | 2412 |
| $V_{SH}$ (m/s) | 2534 | 2520 | 2541 | 2625 |
| $\varepsilon$ (-) | 0,112 | 0,103 | 0,109 | 0,156 |
| $\gamma$ (-) | 0,122 | 0,100 | 0,089 | 0,092 |
| $\delta$ (-) | 0,008 | 0,010 | 0,033 | 0,138 |
| $C_{11}$ (GPa) | 35,28 | 35,23 | 35,92 | 40,56 |
| $C_{33}$ (GPa) | 28,84 | 29,21 | 29,52 | 30,93 |
| $C_{44}$ (GPa) | 13,03 | 13,36 | 13,82 | 14,68 |
| $C_{66}$ (GPa) | 16,19 | 16,02 | 16,28 | 17,38 |
| $C_{13}$ (GPa) | 2,54 | 2,78 | 2,82 | 5,41 |

Table D - 2. List of measured and calculated directional Young's moduli and Poisson's ratios, directional P- and S-wave velocities, Thomsen's anisotropy parameters, and independent elements of anisotropy tensor of Mancos shale RH=12% at seismic (1 Hz, 21 Hz, 105 Hz) and ultrasonic frequencies.

| | 1 (Hz) | 21 (Hz) | 105 (Hz) | ultrasonic |
|---|---|---|---|---|
| $E_V$ (GPa) | 27,69 | 28,46 | 28,65 | 29,97 |
| $E_H$ (GPa) | 34,19 | 34,65 | 35,06 | 38,95 |
| $\nu_{VH}$ (-) | 0,083 | 0,084 | 0,082 | 0,118 |
| $\nu_{HV}$ (-) | 0,104 | 0,107 | 0,107 | 0,154 |
| $\nu_{HH}$ (-) | 0,084 | 0,087 | 0,089 | 0,113 |
| $V_{PV}$ (m/s) | 3333 | 3379 | 3389 | 3507 |
| $V_{PH}$ (m/s) | 3701 | 3726 | 3748 | 3987 |
| $V_{SV}$ (m/s) | 2229 | 2282 | 2315 | 2411 |
| $V_{SH}$ (m/s) | 2491 | 2505 | 2517 | 2624 |
| $\varepsilon$ (-) | 0,116 | 0,108 | 0,112 | 0,146 |
| $\gamma$ (-) | 0,125 | 0,103 | 0,091 | 0,092 |
| $\delta$ (-) | 0,006 | 0,024 | 0,045 | 0,132 |
| $C_{11}$ (GPa) | 34,79 | 35,28 | 35,69 | 40,39 |
| $C_{33}$ (GPa) | 28,22 | 29,00 | 29,18 | 31,25 |
| $C_{44}$ (GPa) | 12,62 | 13,23 | 13,62 | 14,77 |
| $C_{66}$ (GPa) | 15,76 | 15,94 | 16,10 | 17,49 |
| $C_{13}$ (GPa) | 3,16 | 3,24 | 3,21 | 5,41 |

Table D - 3. List of measured and calculated directional Young's moduli and Poisson's ratios, directional P- and S-wave velocities, Thomsen's anisotropy parameters, and independent elements of anisotropy tensor of Mancos shale RH=34% at seismic (1 Hz, 21 Hz, 105 Hz) and ultrasonic frequencies.

| | 1 (Hz) | 21 (Hz) | 105 (Hz) | ultrasonic |
|---|---|---|---|---|
| $E_V$ (GPa) | 25,99 | 27,06 | 27,52 | 28,33 |
| $E_H$ (GPa) | 32,65 | 33,56 | 34,08 | 36,12 |
| $\nu_{VH}$ (-) | 0,092 | 0,095 | 0,099 | 0,146 |
| $\nu_{HV}$ (-) | 0,115 | 0,117 | 0,122 | 0,186 |
| $\nu_{HH}$ (-) | 0,074 | 0,081 | 0,091 | 0,126 |
| $V_{PV}$ (m/s) | 3237 | 3305 | 3337 | 3450 |
| $V_{PH}$ (m/s) | 3619 | 3672 | 3706 | 3873 |
| $V_{SV}$ (m/s) | 2180 | 2242 | 2274 | 2309 |
| $V_{SH}$ (m/s) | 2447 | 2473 | 2480 | 2514 |
| $\varepsilon$ (-) | 0,125 | 0,117 | 0,117 | 0,130 |
| $\gamma$ (-) | 0,130 | 0,108 | 0,095 | 0,092 |
| $\delta$ (-) | 0,032 | 0,050 | 0,067 | 0,120 |
| $C_{11}$ (GPa) | 33,24 | 34,23 | 34,88 | 38,08 |
| $C_{33}$ (GPa) | 26,60 | 27,73 | 28,27 | 30,21 |
| $C_{44}$ (GPa) | 12,06 | 12,76 | 13,13 | 13,54 |
| $C_{66}$ (GPa) | 15,20 | 15,53 | 15,62 | 16,04 |
| $C_{13}$ (GPa) | 3,31 | 3,54 | 3,81 | 6,44 |

Table D - 4. List of measured and calculated directional Young's moduli and Poisson's ratios, directional P- and S-wave velocities, Thomsen's anisotropy parameters, and independent elements of anisotropy tensor of the Mancos shale RH=55% at seismic (1 Hz, 21 Hz, 105 Hz) and ultrasonic frequencies.

| | 1 (Hz) | 21 (Hz) | 105 (Hz) | ultrasonic |
|---|---|---|---|---|
| $E_V$ (GPa) | 25,81 | 26,67 | 27,17 | 30,94 |
| $E_H$ (GPa) | 33,10 | 33,78 | 34,13 | 38,82 |
| $\nu_{VH}$ (-) | 0,132 | 0,133 | 0,132 | 0,195 |
| $\nu_{HV}$ (-) | 0,169 | 0,168 | 0,166 | 0,245 |
| $\nu_{HH}$ (-) | 0,103 | 0,109 | 0,113 | 0,162 |
| $V_{PV}$ (m/s) | 3255 | 3310 | 3339 | 3692 |
| $V_{PH}$ (m/s) | 3665 | 3705 | 3725 | 4089 |
| $V_{SV}$ (m/s) | 2145 | 2200 | 2236 | 2345 |
| $V_{SH}$ (m/s) | 2419 | 2438 | 2446 | 2553 |
| $\varepsilon$ (-) | 0,134 | 0,127 | 0,122 | 0,113 |
| $\gamma$ (-) | 0,136 | 0,114 | 0,099 | 0,093 |
| $\delta$ (-) | 0,059 | 0,077 | 0,090 | 0,107 |
| $C_{11}$ (GPa) | 34,42 | 35,18 | 35,56 | 42,85 |
| $C_{33}$ (GPa) | 27,16 | 28,08 | 28,58 | 34,93 |
| $C_{44}$ (GPa) | 11,79 | 12,41 | 12,81 | 14,09 |
| $C_{66}$ (GPa) | 15,00 | 15,24 | 15,34 | 16,70 |
| $C_{13}$ (GPa) | 5,11 | 5,30 | 5,34 | 10,21 |

Table D - 5. List of measured and calculated directional Young's moduli and Poisson's ratios, directional P- and S-wave velocities, Thomsen's anisotropy parameters, and independent elements of anisotropy tensor of Mancos shale RH=76% at seismic (1 Hz, 21 Hz, 105 Hz) and ultrasonic frequencies.

| | 1 (Hz) | 21 (Hz) | 105 (Hz) | ultrasonic |
|---|---|---|---|---|
| $E_V$ (GPa) | 24,89 | 26,06 | 26,86 | 32,96 |
| $E_H$ (GPa) | 32,75 | 33,92 | 34,49 | 40,92 |
| $\nu_{VH}$ (-) | 0,212 | 0,218 | 0,223 | 0,254 |
| $\nu_{HV}$ (-) | 0,279 | 0,283 | 0,286 | 0,315 |
| $\nu_{HH}$ (-) | 0,190 | 0,197 | 0,205 | 0,208 |
| $V_{PV}$ (m/s) | 3374 | 3467 | 3535 | 4014 |
| $V_{PH}$ (m/s) | 3824 | 3909 | 3960 | 4387 |
| $V_{SV}$ (m/s) | 2045 | 2112 | 2154 | 2361 |
| $V_{SH}$ (m/s) | 2317 | 2352 | 2364 | 2571 |
| $\varepsilon$ (-) | 0,142 | 0,136 | 0,127 | 0,097 |
| $\gamma$ (-) | 0,142 | 0,120 | 0,102 | 0,093 |
| $\delta$ (-) | 0,085 | 0,103 | 0,111 | 0,096 |
| $C_{11}$ (GPa) | 37,45 | 39,14 | 40,16 | 49,29 |
| $C_{33}$ (GPa) | 29,16 | 30,79 | 32,01 | 41,28 |
| $C_{44}$ (GPa) | 10,72 | 11,43 | 11,88 | 14,28 |
| $C_{66}$ (GPa) | 13,76 | 14,16 | 14,31 | 16,94 |
| $C_{13}$ (GPa) | 10,05 | 10,87 | 11,53 | 16,41 |

Table D - 6. List of measured and calculated directional Young's moduli and Poisson's ratios, directional P- and S-wave velocities, Thomsen's anisotropy parameters, and independent elements of anisotropy tensor of as-received Mancos shale at seismic (1 Hz, 21 Hz, 105 Hz) and ultrasonic frequencies.

| | 1 (Hz) | 21 (Hz) | 105 (Hz) | ultrasonic |
|---|---|---|---|---|
| $E_V$ (GPa) | 24,13 | 25,18 | 26,21 | 32,44 |
| $E_H$ (GPa) | 32,16 | 33,22 | 34,02 | 40,08 |
| $\nu_{VH}$ (-) | 0,242 | 0,241 | 0,243 | 0,274 |
| $\nu_{HV}$ (-) | 0,316 | 0,320 | 0,319 | 0,338 |
| $\nu_{HH}$ (-) | 0,222 | 0,219 | 0,221 | 0,221 |
| $V_{PV}$ (m/s) | 3428 | 3493 | 3565 | 4072 |
| $V_{PH}$ (m/s) | 3896 | 3951 | 4002 | 4421 |
| $V_{SV}$ (m/s) | 1994 | 2065 | 2119 | 2321 |
| $V_{SH}$ (m/s) | 2264 | 2304 | 2329 | 2528 |
| $\varepsilon$ (-) | 0,146 | 0,140 | 0,130 | 0,089 |
| $\gamma$ (-) | 0,144 | 0,122 | 0,104 | 0,093 |
| $\delta$ (-) | 0,097 | 0,115 | 0,121 | 0,090 |
| $C_{11}$ (GPa) | 38,99 | 40,09 | 41,12 | 50,19 |
| $C_{33}$ (GPa) | 30,17 | 31,32 | 32,64 | 42,57 |
| $C_{44}$ (GPa) | 10,21 | 10,95 | 11,53 | 13,84 |
| $C_{66}$ (GPa) | 13,16 | 13,63 | 13,93 | 16,41 |
| $C_{13}$ (GPa) | 12,49 | 12,75 | 13,23 | 18,50 |

Table D - 7. List of measured and calculated directional Young's moduli and Poisson's ratios, directional P- and S-wave velocities, Thomsen's anisotropy parameters, and independent elements of anisotropy tensor of Mancos shale RH=100% at seismic (1 Hz, 21 Hz, 105 Hz) and ultrasonic frequencies.

| | 1 (Hz) | 21 (Hz) | 105 (Hz) | ultrasonic |
|---|---|---|---|---|
| $E_V$ (GPa) | 20,85 | 22,15 | 23,21 | 31,04 |
| $E_H$ (GPa) | 28,32 | 29,96 | 30,83 | 37,99 |
| $\nu_{VH}$ (-) | 0,305 | 0,302 | 0,300 | 0,285 |
| $\nu_{HV}$ (-) | 0,415 | 0,408 | 0,398 | 0,349 |
| $\nu_{HH}$ (-) | 0,300 | 0,286 | 0,277 | 0,218 |
| $V_{PV}$ (m/s) | 3572 | 3631 | 3678 | 4030 |
| $V_{PH}$ (m/s) | 4078 | 4127 | 4139 | 4335 |
| $V_{SV}$ (m/s) | 1811 | 1906 | 1971 | 2265 |
| $V_{SH}$ (m/s) | 2062 | 2132 | 2170 | 2467 |
| $\varepsilon$ (-) | 0,152 | 0,146 | 0,133 | 0,079 |
| $\gamma$ (-) | 0,148 | 0,126 | 0,106 | 0,093 |
| $\delta$ (-) | 0,114 | 0,132 | 0,136 | 0,082 |
| $C_{11}$ (GPa) | 42,60 | 43,64 | 43,90 | 48,16 |
| $C_{33}$ (GPa) | 32,68 | 33,79 | 34,66 | 41,61 |
| $C_{44}$ (GPa) | 8,40 | 9,31 | 9,95 | 13,14 |
| $C_{66}$ (GPa) | 10,89 | 11,65 | 12,07 | 15,59 |
| $C_{13}$ (GPa) | 19,37 | 19,29 | 19,09 | 18,55 |

Table D - 8. List of measured and calculated directional Young's moduli and Poisson's ratios, directional P- and S-wave velocities, Thomsen's anisotropy parameters, and independent elements of anisotropy tensor of Pierre shale RH=19% at seismic (1 Hz, 21 Hz, 105 Hz) and ultrasonic frequencies.

| | 1 (Hz) | 21 (Hz) | 105 (Hz) | ultrasonic |
|---|---|---|---|---|
| $E_V$ (GPa) | 12,61 | 13,28 | 13,72 | 14,84 |
| $E_H$ (GPa) | 19,20 | 19,79 | 20,09 | 21,54 |
| $\nu_{VH}$ (-) | 0,105 | 0,103 | 0,104 | 0,080 |
| $\nu_{HV}$ (-) | 0,159 | 0,157 | 0,158 | 0,116 |
| $\nu_{HH}$ (-) | 0,100 | 0,100 | 0,103 | 0,087 |
| $V_{PV}$ (m/s) | 2388 | 2448 | 2488 | 2568 |
| $V_{PH}$ (m/s) | 2936 | 2979 | 3003 | 3091 |
| $V_{SV}$ (m/s) | 1774 | 1778 | 1792 | 1810 |
| $V_{SH}$ (m/s) | 1949 | 1980 | 1992 | 2076 |
| $\varepsilon$ (-) | 0,256 | 0,241 | 0,228 | 0,224 |
| $\gamma$ (-) | 0,104 | 0,120 | 0,118 | 0,158 |
| $\delta$ (-) | 0,371 | 0,279 | 0,250 | 0,135 |
| $C_{11}$ (GPa) | 19,81 | 20,39 | 20,72 | 21,94 |
| $C_{33}$ (GPa) | 13,10 | 13,76 | 14,22 | 15,14 |
| $C_{44}$ (GPa) | 7,23 | 7,26 | 7,38 | 7,53 |
| $C_{66}$ (GPa) | 8,73 | 9,00 | 9,11 | 9,90 |
| $C_{13}$ (GPa) | 2,33 | 2,34 | 2,41 | 1,92 |

Table D - 9. List of measured and calculated directional Young's moduli and Poisson's ratios, directional P- and S-wave velocities, Thomsen's anisotropy parameters, and independent elements of anisotropy tensor of Pierre shale RH=34% at seismic (1 Hz, 21 Hz, 105 Hz) and ultrasonic frequencies.

| | 1 (Hz) | 21 (Hz) | 105 (Hz) | ultrasonic |
|---|---|---|---|---|
| $E_V$ (GPa) | 11,96 | 12,41 | 12,73 | 13,95 |
| $E_H$ (GPa) | 18,01 | 18,52 | 18,70 | 20,06 |
| $\nu_{VH}$ (-) | 0,111 | 0,108 | 0,109 | 0,071 |
| $\nu_{HV}$ (-) | 0,167 | 0,161 | 0,160 | 0,102 |
| $\nu_{HH}$ (-) | 0,104 | 0,102 | 0,104 | 0,053 |
| $V_{PV}$ (m/s) | 2310 | 2349 | 2379 | 2461 |
| $V_{PH}$ (m/s) | 2823 | 2860 | 2875 | 2944 |
| $V_{SV}$ (m/s) | 1699 | 1711 | 1726 | 1754 |
| $V_{SH}$ (m/s) | 1868 | 1895 | 1903 | 2018 |
| $\varepsilon$ (-) | 0,247 | 0,241 | 0,230 | 0,216 |
| $\gamma$ (-) | 0,105 | 0,114 | 0,108 | 0,162 |
| $\delta$ (-) | 0,347 | 0,302 | 0,287 | 0,139 |
| $C_{11}$ (GPa) | 18,64 | 19,13 | 19,33 | 20,28 |
| $C_{33}$ (GPa) | 12,48 | 12,91 | 13,24 | 14,17 |
| $C_{44}$ (GPa) | 6,75 | 6,85 | 6,97 | 7,20 |
| $C_{66}$ (GPa) | 8,16 | 8,40 | 8,47 | 9,52 |
| $C_{13}$ (GPa) | 2,33 | 2,32 | 2,36 | 1,53 |

Table D - 10. List of measured and calculated directional Young's moduli and Poisson's ratios, directional P- and S-wave velocities, Thomsen's anisotropy parameters, and independent elements of anisotropy tensor of Pierre shale RH=55% at seismic (1 Hz, 21 Hz, 105 Hz) and ultrasonic frequencies.

| | 1 (Hz) | 21 (Hz) | 105 (Hz) | ultrasonic |
|---|---|---|---|---|
| $E_V$ (GPa) | 11,47 | 11,65 | 11,87 | 14,06 |
| $E_H$ (GPa) | 17,07 | 17,56 | 17,70 | 20,14 |
| $\nu_{VH}$ (-) | 0,160 | 0,165 | 0,172 | 0,170 |
| $\nu_{HV}$ (-) | 0,227 | 0,233 | 0,240 | 0,244 |
| $\nu_{HH}$ (-) | 0,154 | 0,159 | 0,164 | 0,147 |
| $V_{PV}$ (m/s) | 2316 | 2344 | 2376 | 2575 |
| $V_{PH}$ (m/s) | 2805 | 2854 | 2876 | 3050 |
| $V_{SV}$ (m/s) | 1611 | 1634 | 1652 | 1673 |
| $V_{SH}$ (m/s) | 1774 | 1796 | 1798 | 1933 |
| $\varepsilon$ (-) | 0,233 | 0,241 | 0,233 | 0,202 |
| $\gamma$ (-) | 0,106 | 0,104 | 0,093 | 0,168 |
| $\delta$ (-) | 0,310 | 0,338 | 0,346 | 0,145 |
| $C_{11}$ (GPa) | 18,49 | 19,14 | 19,44 | 21,86 |
| $C_{33}$ (GPa) | 12,61 | 12,91 | 13,26 | 15,58 |
| $C_{44}$ (GPa) | 6,10 | 6,27 | 6,41 | 6,58 |
| $C_{66}$ (GPa) | 7,40 | 7,58 | 7,60 | 8,78 |
| $C_{13}$ (GPa) | 3,55 | 3,83 | 4,07 | 4,46 |

Table D - 11. List of measured and calculated directional Young's moduli and Poisson's ratios, directional P- and S-wave velocities, Thomsen's anisotropy parameters, and independent elements of anisotropy tensor of Pierre shale RH=76% at seismic (1 Hz, 21 Hz, 105 Hz) and ultrasonic frequencies.

| | 1 (Hz) | 21 (Hz) | 105 (Hz) | ultrasonic |
|---|---|---|---|---|
| $E_V$ (GPa) | 10,50 | 11,08 | 11,55 | 16,32 |
| $E_H$ (GPa) | 15,58 | 17,13 | 17,80 | 23,50 |
| $\nu_{VH}$ (-) | 0,236 | 0,238 | 0,248 | 0,244 |
| $\nu_{HV}$ (-) | 0,350 | 0,368 | 0,382 | 0,352 |
| $\nu_{HH}$ (-) | 0,235 | 0,223 | 0,225 | 0,212 |
| $V_{PV}$ (m/s) | 2360 | 2440 | 2520 | 2946 |
| $V_{PH}$ (m/s) | 2833 | 2972 | 3056 | 3458 |
| $V_{SV}$ (m/s) | 1469 | 1565 | 1616 | 1731 |
| $V_{SH}$ (m/s) | 1620 | 1707 | 1738 | 2008 |
| $\varepsilon$ (-) | 0,220 | 0,242 | 0,235 | 0,189 |
| $\gamma$ (-) | 0,108 | 0,095 | 0,079 | 0,173 |
| $\delta$ (-) | 0,277 | 0,371 | 0,399 | 0,151 |
| $C_{11}$ (GPa) | 19,29 | 21,23 | 22,46 | 28,75 |
| $C_{33}$ (GPa) | 13,39 | 14,31 | 15,27 | 20,87 |
| $C_{44}$ (GPa) | 5,19 | 5,89 | 6,28 | 7,20 |
| $C_{66}$ (GPa) | 6,31 | 7,01 | 7,26 | 9,70 |
| $C_{13}$ (GPa) | 6,12 | 6,78 | 7,53 | 9,31 |